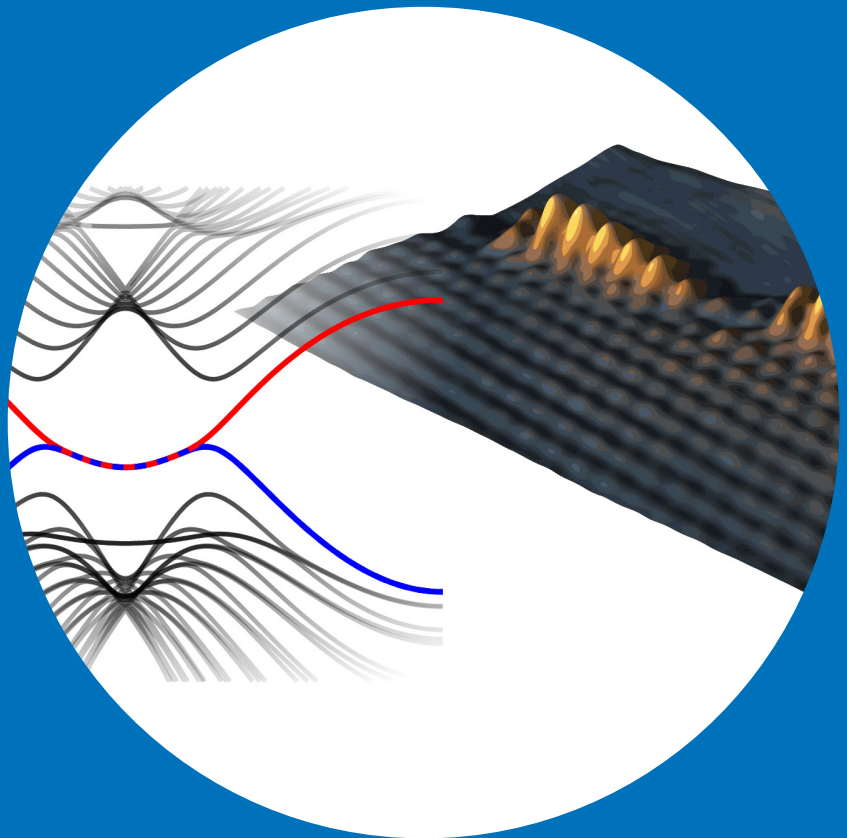


Department of Applied Physics

Electronic properties of graphene from tight-binding simulations

Andreas Uppstu



Electronic properties of graphene from tight-binding simulations

Andreas Uppstu

A doctoral dissertation completed for the degree of Doctor of Science (Technology) to be defended, with the permission of the Aalto University School of Science, at a public examination held at lecture hall M1 (Otakaari 1, Espoo) of the school on 12 September 2014 at 13.

Aalto University
School of Science
Department of Applied Physics

Supervising professor

Aalto Distinguished Professor Risto Nieminen

Thesis advisor

Adjunct Professor Ari Harju

Preliminary examiners

Doctor Jani Kotakoski, University of Vienna, Austria

Professor Igor Zozoulenko, Linköping University, Sweden

Opponent

Professor Oleg Yazyev, École Polytechnique Fédérale de Lausanne,
Switzerland

Aalto University publication series

DOCTORAL DISSERTATIONS 122/2014

© Andreas Uppstu

ISBN 978-952-60-5814-6

ISBN 978-952-60-5815-3 (pdf)

ISSN-L 1799-4934

ISSN 1799-4934 (printed)

ISSN 1799-4942 (pdf)

<http://urn.fi/URN:ISBN:978-952-60-5815-3>

Unigrafia Oy

Helsinki 2014

Finland



Author

Andreas Uppstu

Name of the doctoral dissertation

Electronic properties of graphene from tight-binding simulations

Publisher School of Science

Unit Department of Applied Physics

Series Aalto University publication series DOCTORAL DISSERTATIONS 122/2014

Field of research Theoretical and computational Physics

Manuscript submitted 12 May 2014

Date of the defence 12 September 2014

Permission to publish granted (date) 18 June 2014

Language English

Monograph

Article dissertation (summary + original articles)

Abstract

Graphene is an effectively two-dimensional semimetallic material consisting of a sheet of carbon atoms arranged in a hexagonal lattice. Due to its high electron mobility and special electronic properties, it is considered to be a promising candidate for various future electronic applications. Freestanding graphene was discovered as late as in 2004, but since then it has become the focus of numerous studies, sparking not only scientific but also significant commercial interest.

Realizing the potential of the material requires both theoretical, numerical, and experimental studies. An important computational model for studying the electronic properties of graphene is the so-called tight-binding (TB) model. In the TB model, the charge carriers of a material are described using effective parameters, which can be either derived from more complex models or fitted to experimental or computational results.

In this Thesis, the TB model was used to study both the local density of states (LDOS) of graphene as well as electronic transport in graphene. Simulating the LDOS of graphene is important, since it may be more or less directly measured using scanning tunneling microscopy (STM), and is thus extremely helpful for characterizing the properties of nanometer-sized graphene samples. The results presented in this Thesis, which show good agreement between simulations and STM measurements, help to determine the electronic structure of graphene quantum dots on various substrates.

Simulations of electronic transport aid in making graphene useful for semiconductor applications. Graphene may be turned semiconducting by various means, such as by cutting it into ribbons or by adding disorder. In this Thesis, it was showed how scaling theory can be utilized to obtain the conductance of a mesoscopically sized disordered graphene device using first-principles-based results and how the localization length of the charge carriers can be obtained effectively using the so-called Kubo-Greenwood method. The results aid in interpreting experimental conductance measurements and in estimating how strong disorder is required to turn graphene into an effective semiconductor.

Keywords graphene, tight-binding, electronic transport, scanning tunneling microscopy

ISBN (printed) 978-952-60-5814-6

ISBN (pdf) 978-952-60-5815-3

ISSN-L 1799-4934

ISSN (printed) 1799-4934

ISSN (pdf) 1799-4942

Location of publisher Helsinki

Location of printing Helsinki

Year 2014

Pages 170

urn <http://urn.fi/URN:ISBN:978-952-60-5815-3>

Författare

Andreas Uppstu

Doktorsavhandlingens titel

Grafens elektroniska egenskaper från starkbindningssimuleringar

Utgivare Högskolan för teknikvetenskaper**Enhet** Avdelningen för teknisk fysik**Seriens namn** Aalto University publication series DOCTORAL DISSERTATIONS 122/2014**Forskningsområde** Teoretisk och numerisk fysik**Inlämningsdatum för manuskript** 12.05.2014 **Datum för disputation** 12.09.2014**Beviljande av publiceringstillstånd (datum)** 18.06.2014 **Språk** Engelska **Monografi** **Sammanläggningsavhandling (sammandrag plus separata artiklar)****Sammandrag**

Grafen är ett effektivt tvådimensionellt material som består av kolatomer arrangerade i ett hexagonalt gitter. Tack vare speciella elektroniska egenskaper, som laddningsbärarnas höga mobilitet, anses grafen vara en lovande kandidat för framtida elektroniska tillämpningar. Fristående grafen upptäcktes så sent som 2004, men sedan dess har materialet blivit fokus för otaliga studier. Förutom ett vetenskapligt intresse, har grafen under den senaste tiden också skapat ett betydande kommersiellt intresse.

För att förverkliga materialets potential krävs både teoretiska, numeriska och experimentella studier. Den så kallade starkbindningsmodellen är en viktig numerisk modell för simulering av grafen. I starkbindningsmodellen beskrivs laddningsbärarna med hjälp av effektiva parametrar, som kan härledas med hjälp av mera komplexa numeriska metoder eller genom att anpassa dem till experimentella resultat.

I denna avhandling används starkbindningsmodellen till att simulera både lokal tillståndstäthet samt elektronisk transport i grafen. Att simulera lokal tillståndstäthet är viktigt, eftersom den kan mer eller mindre direkt mätas genom sveptunnelmikroskopi. Därmed är metoden extremt användbar för att karakterisera nanometerstora grafenflagor. Resultaten som presenteras i denna avhandling visar att simuleringarna stämmer bra överens med experimentella resultat.

Simuleringar av elektronisk transport kan hjälpa med att få grafen användbart för halvledarapplikationer. Grafen kan fås till att bli en halvledare med olika metoder, till exempel genom att skära den i strimlor eller lägga till ordning i det annars perfekta gittret. I denna avhandling visas hur man kan använda ab initio -baserade metoder för att beräkna grafens konduktans och hur den så kallade Kubo-Greenwood-metoden kan användas till att beräkna laddningsbärarnas lokaliseringslängd. Dessa resultat hjälper att tolka experimentella mätresultat och att estimerar hur stark ordning krävs för att ändra grafen till en effektiv halvledare.

Nyckelord grafen, starkbindning, elektronisk transport, sveptunnelmikroskopi**ISBN (tryckt)** 978-952-60-5814-6**ISBN (pdf)** 978-952-60-5815-3**ISSN-L** 1799-4934**ISSN (tryckt)** 1799-4934**ISSN (pdf)** 1799-4942**Utgivningsort** Helsingfors**Tryckort** Helsingfors**År** 2014**Sidantal** 170**urn** <http://urn.fi/URN:ISBN:978-952-60-5815-3>

Preface

This work has been performed in the Quantum Many-Body Physics group, led by my instructor Dr. Ari Harju. I want to thank Ari for helpful discussions and all of his support, as well as all of the the current and past members of the group for creating a nice working environment. I want to thank my supervisor, Prof. Risto Nieminen, for giving me the opportunity to work at the Academy of Finland Center of Excellence in Computational Nanoscience. I also want to thank all of my co-authors, many of whom work in collaborating groups led by Professors Pertti Hakonen, Peter Liljeroth, Martti Puska, Ingmar Swart and Daniel Vanmaekelbergh. I want to specifically thank Prof. Peter Liljeroth for giving me the opportunity to continue working at the university for a while, and my co-worker Mikko Ervasti for making coffee almost every working day.

Espoo, August 13, 2014,

Andreas Uppstu

Contents

Preface	1
Contents	3
List of Publications	5
Author's Contribution	7
1. Introduction	11
2. Computational methods	15
2.1 The tight-binding model	15
2.2 The Hubbard model	17
2.3 Density functional theory	18
2.4 Methods for computing the local density of states	19
2.5 Methods for transport calculations	20
2.5.1 The Landauer-Büttiker formalism	20
2.5.2 The Kubo-Greenwood method	21
3. The electronic structure of graphene	23
3.1 Band structure	23
3.2 Comparisons between simulations and scanning tunneling microscopy results	27
4. Electronic transport in graphene	31
4.1 Ballistic transport and Fabry-Pérot resonances	31
4.2 Transport in disordered graphene	33
4.3 Effective scattering cross-section formalism	35
4.4 Electronic transport in a magnetic field	40
4.5 Spin-dependent transport	41
4.6 Phonon-assisted transport	43
5. Summary	47
Bibliography	51
Publications	55

List of Publications

This thesis consists of an overview and of the following publications which are referred to in the text by their Roman numerals.

- I** Y. Hancock, A. Uppstu, K. Saloriutta, A. Harju and M. J. Puska. Generalized tight-binding transport model for graphene nanoribbon-based systems. *Physical Review B*, **81**, 245402, 2010.
- II** J. van der Lit, M. P. Boneschanscher, D. Vanmaekelbergh, M. Ijäs, A. Uppstu, M. Ervasti, A. Harju, P. Liljeroth and I. Swart. Suppression of electron-vibron coupling in graphene nanoribbons contacted via a single atom. *Nature Communications*, **4**, 2023, 2013.
- III** M. Ijäs, M. Ervasti, A. Uppstu, P. Liljeroth, J. van der Lit, I. Swart, and A. Harju. Electronic states in finite graphene nanoribbons: Effect of charging and defects. *Physical Review B*, **88**, 075429, 2013.
- IV** S. K. Hämäläinen, Z. Sun, M. P. Boneschanscher, A. Uppstu, M. Ijäs, A. Harju, D. Vanmaekelbergh, and Peter Liljeroth. Quantum-Confined Electronic States in Atomically Well-Defined Graphene Nanostructures. *Physical Review Letters*, **107**, 236803, 2011.
- V** R. Drost, A. Uppstu, F. Schulz, S. K. Hämäläinen, M. Ervasti, A. Harju, and P. Liljeroth. Electronic States at the Graphene - Hexagonal Boron Nitride Zigzag Interface. Accepted for publication in *Nano Letters*, July 2014.
- VI** Z. Fan, A. Uppstu, T. Siro and A. Harju. Efficient linear-scaling quantum transport calculations on graphics processing units and applications on electron transport in graphene. *Computer Physics Communications*, **185**, 28, 2014.
- VII** M. Oksanen, A. Uppstu, A. Laaksonen, D. J. Cox, M. F. Craciun, S. Russo, A. Harju and P. Hakonen. Single-mode and multimode Fabry-Perot resonances in graphene. *Physical Review B*, **89**, 121414(R), 2014.
- VIII** A. Uppstu, Z. Fan and A. Harju. Obtaining localization properties effectively using the Kubo-Greenwood formalism. *Physical Review B*, **89**, 075420, 2014.

- IX** A. Uppstu, K. Saloriutta, A. Harju, M. Puska and A.-P. Jauho. Electronic transport in graphene-based structures: An effective cross-section approach. *Physical Review B*, **85**, 041401(R), 2012.
- X** K. Saloriutta, A. Uppstu, A. Harju and M. J. Puska. Ab initio transport fingerprints for resonant scattering in graphene. *Physical Review B*, **86**, 235417, 2012.
- XI** A. Uppstu and A. Harju. High-field magnetoresistance revealing scattering mechanisms in graphene. *Physical Review B*, **86**, 201409(R), 2012.
- XII** Y. Hancock, K. Saloriutta, A. Uppstu, A. Harju and M. J. Puska. Spin-Dependence in Asymmetric, V-Shaped-Notched Graphene Nanoribbons. *Journal of Low Temperature Physics*, **153**, 393, 2008.

Author's Contribution

Publication I: “Generalized tight-binding transport model for graphene nanoribbon-based systems”

The author wrote the first draft of the manuscript and performed the tight-binding calculations.

Publication II: “Suppression of electron-vibron coupling in graphene nanoribbons contacted via a single atom”

The author participated in interpreting the experimental results and performing the computational simulations by writing the transport code.

Publication III: “Electronic states in finite graphene nanoribbons: Effect of charging and defects”

The author performed the Hubbard mean-field calculations and participated in discussing and interpreting the results.

Publication IV: “Quantum-Confined Electronic States in Atomically Well-Defined Graphene Nanostructures”

The author performed the tight-binding calculations for the large flakes and participated in interpreting the experimental results.

Publication V: “Electronic States at the Graphene - Hexagonal Boron Nitride Zigzag Interface”

The author performed the tight-binding calculations and participated in discussing and interpreting the experimental results.

Publication VI: “Efficient linear-scaling quantum transport calculations on graphics processing units and applications on electron transport in graphene”

The author performed the tight-binding calculations and participated in discussing the results.

Publication VII: “Single-mode and multimode Fabry-Perot resonances in graphene”

The author wrote most of the manuscript (excluding the supplementary material), performed the computational simulations and participated in analyzing the experimental data.

Publication VIII: “Obtaining localization properties effectively using the Kubo-Greenwood formalism”

The author wrote the first draft of the manuscript, performed most of the tight-binding simulations and participated in interpreting the results.

Publication IX: “Electronic transport in graphene-based structures: An effective cross-section approach”

The author performed all tight-binding calculations and wrote the first draft of the manuscript.

Publication X: “Ab initio transport fingerprints for resonant scattering in graphene”

The author came up with the main idea for the study, performed a part of the tight-binding calculations and participated in discussing the results.

Publication XI: “High-field magnetoresistance revealing scattering mechanisms in graphene”

The author wrote the manuscript and performed all calculations.

**Publication XII: “Spin-Dependence in Asymmetric,
V-Shaped-Notched Graphene Nanoribbons”**

The author came up with the idea for the manuscript, performed all tight-binding calculations and wrote the first draft of the manuscript.

1. Introduction

Graphene is an effectively two-dimensional material formed by a sheet of carbon atoms arranged into a hexagonal lattice. As it exhibits very special electronic and mechanical properties, an enormous scientific and commercial interest has grown around the material during the recent years. Freestanding graphene was discovered as recently as in 2004 by Andre Geim and Konstantin Novoselov [1], which earned them the Nobel Prize in Physics 2010. However, prior to this, graphene had already been synthesized on top of various substrates [2, 3]. As it is closely related to graphite, and due to its peculiar electronic properties, it had also been studied theoretically and computationally already since 1947 [4].

In the graphene lattice, the four valence electrons of carbon are arranged into σ and π bonds [5]. The energy bands that correspond to the π bonds intersect conically at the charge neutrality point, which gives rise to unique electronic features, such as the half-integer quantum Hall effect [6, 7]. The conical intersections occur at the corners of the hexagonal Brillouin zone, which leads to the formation of two inequivalent valleys in the electronic band structure. The two fact that a hexagonal lattice consists of two sublattices adds another degree of freedom for the charge carriers. Such a system with two degrees of freedom and a linear dispersion relation can be modeled by a Dirac equation for massless fermions, albeit with an effective velocity of light that equals the Fermi velocity of graphene, i.e. $\sim 10^6$ m/s [5]. The relativistic nature of the charge carriers leads to phenomena such as Klein tunneling and Zitterbewegung [8, 9].

Graphene can be seen as the basic building block of a variety of materials with different dimensionalities, such as quasi-one-dimensional nanoribbons or nanotubes, zero-dimensional fullerenes or three-dimensional graphite [9]. Depending on the edge type, there are two basic kinds of graphene nanoribbons (GNRs), called armchair-edged GNRs (AGNRs)

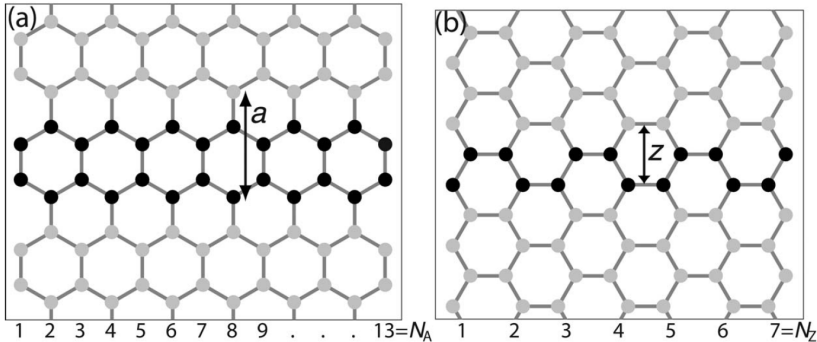


Figure 1.1. Two different edge types of graphene. (a) shows an armchair-edged graphene nanoribbon and (b) a zigzag-edged graphene nanoribbon.

and zigzag-edged GNRs (ZGNRs), while ribbons having intermediate edges are called chiral. The edge types are presented in Fig. 1.1. The edge type has a significant impact on the electronic properties of graphene, as a localized state is formed along the zigzag edge, whereas it is absent along armchair edges [10]. According to computational simulations, the localized edge state of the zigzag edge is susceptible to spin polarization, a feature that has so far not been experimentally unambiguously observed. Experiments have, on the other hand, shown that all GNRs tend to exhibit a transport gap, inversely proportional to the width of the ribbon [11]. The transport gap does usually not equal the band gap, and may e.g. be caused by localization induced by edge disorder [12] or Coulomb blockade [13] originating from a disordered potential background induced by the substrate [14].

In this Thesis, focus is laid on computational simulation of the electronic and transport properties of graphene utilizing models based on the tight-binding (TB) approximation. The parameters of the model are acquired from fitting against first principles results. As shown by comparisons with scanning tunneling microscopy (STM) measurements, TB-based simulations can reproduce experimental results very well, and TB is thus very useful for interpreting various STM measurements. As the main reason for charge carrier scattering in graphene is still debated, TB-based transport simulations may help in interpreting experimental transport measurements. Moreover, such simulations may aid in finding methods to turn graphene into a semiconductor, which is essential for creating graphene-based electronic devices.

The Thesis is organized as follows. Chapter 2 presents the main numerical methods that have been used. In Chapter 3, the electronic structure of

graphene is discussed. In Publication I, TB models for graphene are presented, suitable for both band structure and electronic transport calculations. In Publications II to V, both TB and density-functional-theory-based results are compared against scanning tunneling microscopy measurements of graphene-based systems. Chapter 4 deals with electronic transport in graphene. In Publication VI, two TB-based methods for transport calculations are compared, namely the Landauer-Büttiker and the Kubo-Greenwood formalisms, and efficient methods to implement the Kubo-Greenwood method on GPUs are presented. Publication VIII deals with how the localization length of a mesoscopic conductor can be obtained using the Kubo-Greenwood formalism. In Publication VII, Fabry-Pérot interference in a graphene device is studied both experimentally and computationally. In Publication IX and Publication X an effective scattering cross section formalism for transport calculations in graphene is studied. In Publication XI, electronic transport in the quantum Hall regime is studied, and in Publication XII transport results for notched spin-polarized ZGNRs are presented.

2. Computational methods

2.1 The tight-binding model

The TB model is a very simple model for electronic structure calculations. Its advantage over *ab initio* methods is its low computational cost, which enables simulating systems that are large enough to contain even millions of atoms. Despite the simplicity of the model, it is relatively accurate, especially for carbon-based materials such as graphene.

In the TB model, the total wave function of a system is approximated to be a linear combination of atomic orbitals centered on the atomic sites of the lattice. The model can be further simplified by only simulating charge carriers with energies close to the Fermi level. For example, each carbon atom has four valence electrons, but in graphene they are arranged in three planar σ bonds and a single π bond, distributed equally over the neighbors. In graphene, the electronic states closest to the charge neutrality point (CNP) correspond to the π bonds, and thus it is sufficient to model only a single π electron per atomic site [15].

The Hamiltonian for an electron occupying a lattice point can be written as

$$H = H_{at} + \Delta V(\mathbf{r}), \quad (2.1)$$

where H_{at} is the atomic Hamiltonian and $\Delta V(\mathbf{r})$ is the potential caused by all the other ions of the lattice. Let $\psi_n(\mathbf{r})$ denote an eigenstate of the atomic Hamiltonian, i.e. an atomic orbital, thus satisfying

$$H_{at}\psi_n(\mathbf{r}) = E_n\psi_n(\mathbf{r}). \quad (2.2)$$

An electronic state $\Psi(\mathbf{r})$ localized at the atomic site can be expressed as a

linear combination of the atomic orbitals, according to

$$\Psi(\mathbf{r}) = \sum_n b_n \psi_n(\mathbf{r}), \quad (2.3)$$

where b_n denotes the expansion coefficients. These electronic states can further be expanded to form a Bloch wave that satisfies the periodicity of the lattice, defined by the lattice vectors \mathbf{R} ,

$$\Phi(\mathbf{r}) = \sum_{\mathbf{R}} \exp(i\mathbf{k} \cdot \mathbf{r}) \Psi(\mathbf{r} - \mathbf{R}), \quad (2.4)$$

where \mathbf{k} is the crystal momentum. This can be taken to be the solution of a Schrödinger equation with the Hamiltonian defined by Eq. 2.1, i.e.

$$H\Phi(\mathbf{r}) = H_{at}\Phi(\mathbf{r}) + \Delta V(\mathbf{r})\Phi(\mathbf{r}) = E(\mathbf{k})\Phi(\mathbf{r}). \quad (2.5)$$

By multiplying with $\psi^*(\mathbf{r})$ and integrating over \mathbf{r} this turns into the matrix equation

$$\sum_n A(\mathbf{k})_{mn} b_n = E(\mathbf{k}) \sum_n B(\mathbf{k})_{mn} b_n, \quad (2.6)$$

where the matrices A and B are defined as

$$A(\mathbf{k})_{mn} = \sum_{\mathbf{R}} \exp(i\mathbf{k} \cdot \mathbf{R}) \int \psi_m^*(\mathbf{r}) H \psi_n(\mathbf{r} - \mathbf{R}) d\mathbf{r} \quad (2.7)$$

and

$$B(\mathbf{k})_{mn} = \sum_{\mathbf{R}} \exp(i\mathbf{k} \cdot \mathbf{R}) \int \psi_m^*(\mathbf{r}) \psi_n(\mathbf{r} - \mathbf{R}) d\mathbf{r}. \quad (2.8)$$

By inserting Eq. 2.1 and using the orthonormality of the atomic orbitals an equivalent expression can be obtained, i.e.

$$\sum_n C(\mathbf{k})_{mn} b_m = (E(\mathbf{k}) - E_m) \sum_n B(\mathbf{k})_{mn} b_n, \quad (2.9)$$

where the elements of the matrix $C(\mathbf{k})$ are defined as

$$C(\mathbf{k})_{mn} = \sum_{\mathbf{R}} \exp(i\mathbf{k} \cdot \mathbf{R}) \int \psi_m^*(\mathbf{r}) \Delta V(\mathbf{r}) \psi_n(\mathbf{r} - \mathbf{R}) d\mathbf{r}. \quad (2.10)$$

As an abbreviation, the integrals can be denoted as

$$s(\mathbf{R}) = \int \psi^*(\mathbf{r}) \psi(\mathbf{r} - \mathbf{R}) d\mathbf{r} \quad (2.11)$$

and

$$t(\mathbf{R}) = \int \psi^*(\mathbf{r}) \Delta V(\mathbf{r}) \psi(\mathbf{r} - \mathbf{R}) d\mathbf{r}. \quad (2.12)$$

The first integral is commonly called the overlap integral, and the second the hopping integral, as it can be thought to represent the energy cost for a charge carrier to hop from one lattice site to another. The values of both $t(\mathbf{R})$ and $s(\mathbf{R})$ greatly depend on the discrete variable \mathbf{R} . The wave function $\Psi(\mathbf{r})$ decays exponentially away from the lattice site with $\mathbf{R} = 0$, and it is often approximated that $s = 0$ if $\mathbf{R} \neq 0$, which creates an orthogonal TB model. If $\mathbf{R} = 0$, $s(\mathbf{R}) = 1$. In the simplest tight binding model, the hopping integral is assumed to take nonzero values only between nearest neighbors, but also further than nearest neighbor interactions may be considered.

2.2 The Hubbard model

The basic TB model describes non-interacting particles. Thus, in order to simulate phenomena like spin polarization, one may add an interaction term into the Hamiltonian. The so-called Hubbard model provides one of the simplest ways to implement this, by taking into account the Coulomb repulsion of the electrons only in the case of the electrons occupying the same lattice site. This allows the study of the basic magnetic properties of graphene-based systems. In the second quantization notion, the Hubbard Hamiltonian can be written as

$$H = \sum_{i,j} t_{i,j} c_i c_j^\dagger + U \sum_{i,\sigma} n_{i,\sigma} n_{i,-\sigma}, \quad (2.13)$$

where c and c^\dagger are the electronic creation and annihilation operators, i and j are site indices, and U is a parameter describing the strength of the electronic on-site Coulomb repulsion. $n_{i,\sigma}$ and $n_{i,-\sigma}$ are the number operators for the opposite spins σ and $-\sigma$. Despite the simplicity of the Hubbard model, it can only be used to study systems that contain a handful of lattice sites, as the dimension of the many-body Hilbert space grows roughly exponentially with system size. In order to study larger systems, one may apply the mean field approximation, which effectively reduces the interparticle interactions into interactions between a single particle and a field caused by all the other particles. It is derived as follows.

The fluctuation of the spin density from the mean value $\langle n_{i,\sigma} \rangle$ is given by

$$\Delta n_{i,\sigma} = \langle n_{i,\sigma} \rangle - n_{i,\sigma}, \quad (2.14)$$

and the Hubbard term can thus be written as

$$\begin{aligned} & U \sum_{i,\sigma} (\langle n_{i,\sigma} \rangle - \Delta n_{i,\sigma}) (\langle n_{i,-\sigma} \rangle - \Delta n_{i,-\sigma}) \\ = & U \sum_{i,\sigma} (\langle n_{i,\sigma} \rangle \langle n_{i,-\sigma} \rangle - \langle n_{i,\sigma} \rangle \Delta n_{i,-\sigma} - \langle n_{i,-\sigma} \rangle \Delta n_{i,\sigma} + \Delta n_{i,\sigma} \Delta n_{i,-\sigma}). \end{aligned} \quad (2.15)$$

If the fluctuations are assumed to be small, the last term can be ignored. After re-insertion of Eq. 2.14, the final form of the mean field Hubbard Hamiltonian is acquired

$$H = \sum_{i,j} t_{i,j} c_i c_j^\dagger + U \sum_{i,\sigma} (n_{i,\sigma} \langle n_{i,-\sigma} \rangle + n_{i,-\sigma} \langle n_{i,\sigma} \rangle - \langle n_{i,\sigma} \rangle \langle n_{i,-\sigma} \rangle). \quad (2.16)$$

As the Hamiltonian is needed to obtain the spin occupancies, it must be solved self-consistently, starting with a randomly chosen spin distribution. As the converged result does not necessarily represent the ground state, the computations need to be performed several times in order to ensure that the ground state is found. After a converged ground state result has been acquired, the spin polarization p_i at a lattice site i may be calculated using the expression

$$p_i = \frac{\langle n_{i,\sigma} \rangle - \langle n_{i,-\sigma} \rangle}{\langle n_{i,\sigma} \rangle + \langle n_{i,-\sigma} \rangle}. \quad (2.17)$$

2.3 Density functional theory

The density functional theory (DFT) is an *ab initio* model that can be used to compute the electronic structure of various systems. The foundations of the DFT are laid by the two Hohenberg-Kohn theorems [16]. According to the first one, the electronic density n uniquely determines the electronic properties of the system. Thus the number of degrees of freedom of an N -particle system may be reduced from three times N to three. The second Hohenberg-Kohn theorem states that the exact ground state minimizes the total energy, which is a functional of the electronic density. In order to compute n , the so-called Kohn-Sham framework is used [17]. The framework is based on a Hamiltonian for non-interacting electrons,

which move in an effective potential background that takes into account electron-electron interactions. The potential background is a functional of the electronic density, although the choice of the functional is not completely unambiguous.

The DFT is applied by constructing the Kohn-Sham (K-S) Hamiltonian [17]. It can be used to solve the total energy of the system, as well as the self-consistent electronic density. However, the physical meaning of the individual K-S eigenvalues and eigenstates has not been rigorously justified, although the energy of the highest occupied eigenstate has been shown to be related to the first ionization energy [18]. Nevertheless, as comparisons with scanning tunneling microscopy measurements have shown, the individual K-S eigenstates bear a clear similarity with experimental dI/dV maps.

2.4 Methods for computing the local density of states

The local density of states (LDOS) is defined as the number of electronic states per volume and energy element. Scanning tunneling microscopy provides a method to measure the LDOS experimentally, and experimental results may be directly compared to the simulated LDOS maps. To obtain the LDOS maps, one may compute the retarded Green's function for the system, i.e.

$$\mathcal{G}(E) = \frac{1}{EI - H + i\eta}, \quad (2.18)$$

where I is the identity matrix and η a small positive number, whose magnitude determines the broadening of the states in energy. The LDOS at atomic site i can be obtained from the diagonal elements of the Green's function using the expression

$$\rho_i(E) = -\frac{1}{\pi} \text{Im} \mathcal{G}_{ii}(E) \quad (2.19)$$

Alternatively, if a finite or a periodic system is studied, one may directly diagonalize the corresponding Hamiltonian. To compare the discrete eigenvalue spectrum obtained from diagonalization with experimental results, each eigenvalue is broadened using a Lorentzian function, which creates equivalent results compared with the Green's function method. One has to note that the experimentally measured values are affected by the lifetime broadening of the charge carriers, as well as the layout of the experimental setup, and the broadening parameter may simply be fitted

with the experimental results. In the case of small finite systems, one may obtain a local density of states by means of exact diagonalization of a many-body Hamiltonian. In Publication II and Publication III, the local densities of states for finite seven-atom wide AGNRs, given by the mean-field Hubbard model, the full many-body Hubbard model, and the DFT, are compared with experimental results.

In addition to the TB model, the LDOS can also be approximated using a continuum model. In principle, the correct continuum model for graphene is the Dirac equation, which takes into account all the degrees of freedom of the charge carriers. However, it has been demonstrated that away from the zigzag edges, the LDOS of a hexagonal graphene flake can be fairly accurately estimated also using the scalar Klein-Gordon equation [19]

$$-v_F^2 \hbar^2 \nabla^2 \psi_i = E_i^2 \psi_i, \quad (2.20)$$

where v_F is the Fermi velocity of graphene.

2.5 Methods for transport calculations

2.5.1 The Landauer-Büttiker formalism

The Landauer-Büttiker formalism is a very commonly used method to compute the conductance of a device coupled to two or multiple contacts. An introduction to the formalism can be found e.g. in Ref. [20]. In the Landauer-Büttiker approach, the contacts are modeled as ballistic semi-infinite leads. The conductance is obtained from the transmission function $T(E)$, which for a single mode-system equals the probability of a charge carrier to transmit from one contact to another. If there are several transport modes involved, the transmission function equals the sum of the transmission probabilities for the different modes. The retarded Green's function for a system attached to two leads is given by the expression

$$G(E) = [EI - H - \Sigma_L(E_L) - \Sigma_R(E_R)]^{-1}, \quad (2.21)$$

where I is the unit matrix and $\Sigma_{L/R}(E_{L/R})$ is the self-energy of the corresponding lead. The Fermi energy $E_{L/R}$ of the leads can be set to the same value as in the device, E , or to an arbitrary value. In this work, it is set either to E or to a fixed value of 1.5 eV, which is used to simulate metallic

contacts with a high number of propagating modes. The self energy matrices may be obtained through different methods, e.g., using an iterative method [21]. The matrices $\Gamma_{L/R}$, that describe the coupling to the leads, are obtained from

$$\Gamma_{L/R} = i \left[\Sigma_{L/R} - \Sigma_{L/R}^\dagger \right], \quad (2.22)$$

and the conductance is then computed using

$$G(E) = G_0 \text{Tr} \left[\Gamma_R \mathcal{G}(E) \Gamma_L \mathcal{G}^\dagger(E) \right], \quad (2.23)$$

where $G_0 \equiv 2e^2/h$ is the quantum of conductance.

2.5.2 The Kubo-Greenwood method

The Kubo-Greenwood (KG) method is an alternative method to compute the conductivity of a phase-coherent conductor [22, 23]. In the Kubo-Greenwood formalism, the conductivity is acquired from the expectation value of the mean square displacement (MSD) of the charge carriers. Thus, as opposed to the Landauer-Büttiker formalism, contacts or leads are not modeled. In Publication VI, it is presented how the KG method can be implemented on graphics processing units, together with a comparison with results obtained using the Landauer-Büttiker approach.

The KG formalism is presented in detail in Publication VI, but below is a short summary of the main methods. In the time-dependent Einstein formula [24, 25, 26, 27, 28, 29, 30, 31], which can be derived from the KG formula, the zero-temperature electrical conductivity at Fermi energy E and correlation time t may be obtained as a time-derivative of the MSD $\Delta X^2(E, t)$, i.e.,

$$\sigma(E, t) = e^2 \rho(E) \frac{d}{2dt} \Delta X^2(E, t), \quad (2.24)$$

where

$$\Delta X^2(E, t) = \frac{\text{Tr} \left[\frac{2}{\Omega} \delta(E - H) (X(t) - X)^2 \right]}{\text{Tr} \left[\frac{2}{\Omega} \delta(E - H) \right]}, \quad (2.25)$$

and

$$\rho(E) = \text{Tr} \left[\frac{2}{\Omega} \delta(E - H) \right] \quad (2.26)$$

is the density of states (DOS) with spin degeneracy included. $X(t) = \exp(iHt/\hbar) X \exp(-iHt/\hbar)$ is the position operator X given in the Heisenberg representation. In the case graphene simulations, Ω is the area of the simulation cell.

The KG method has several advantages over the Landauer-Büttiker for-

malism. Perhaps most importantly, one can achieve linear scaling of the computational cost with regard to the simulation cell size, whereas in the GF method the computational cost scales cubically with the width of the system. On the other hand, the KG method has also some drawbacks. Obviously one of them is that the effect of contacts cannot be modeled, only the intrinsic properties of the material. Additionally, in a quasi-1D system, the individual transmission values for different conduction channels cannot be acquired.

3. The electronic structure of graphene

3.1 Band structure

The π electron bands of two-dimensional graphene contain valleys having linear dispersion and being located at the corners of the hexagonal Brillouin zone. Two of the valleys are nonequivalent, creating a valley degree of freedom for the charge carriers. Due to these features, the charge carriers behave as massless Dirac fermions close to the CNP. Figure 3.1 shows the band structure of graphene given by a nearest-neighbor TB calculation and Figure 3.2 shows a zoom-in on the band structure at one of the valleys. The band structure of graphene can be simulated using the DFT, and the TB parameters can then be optimized against the results. In Publication I different sets of TB parameters are presented, suitable for modeling both the band structure and electronic transport properties of GNRs.

As shown in Publication I and Ref. [15], an extended TB model is able to provide results that are very similar to those acquired from much more time consuming *ab initio* calculations. The results still depend highly on the parameters that have been selected, and different sets of parameters can reproduce the band structure of AGNRs and ZGNRs with different degrees of accuracy. In Publication I also electronic transport results given by TB and DFT are compared, more of which will be discussed in Chapter 4.

If graphene is cut into ribbons, the 2D electronic bands become split into sub-bands due to transverse quantization of the energy. In AGNRs, this leads to the formation of a band gap that is inversely proportional to the width of the ribbon [32]. This is illustrated in Fig. 3.3, which shows the band structure of a 14-AGNR, as well as the band gaps of a range of AG-

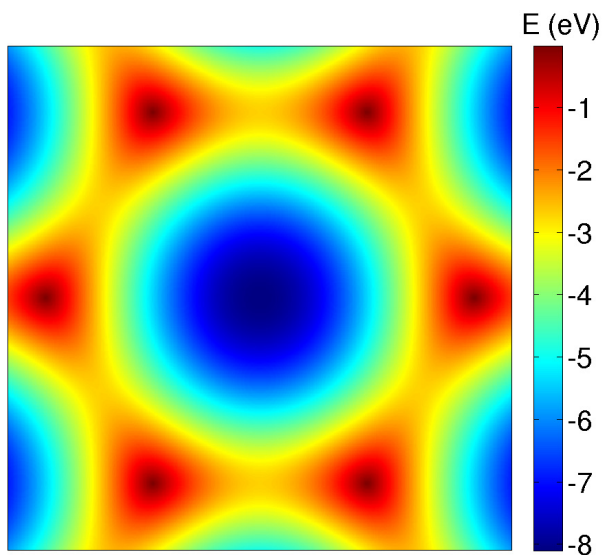


Figure 3.1. The valence band of 2D graphene, computed using a nearest-neighbor tight-binding model.

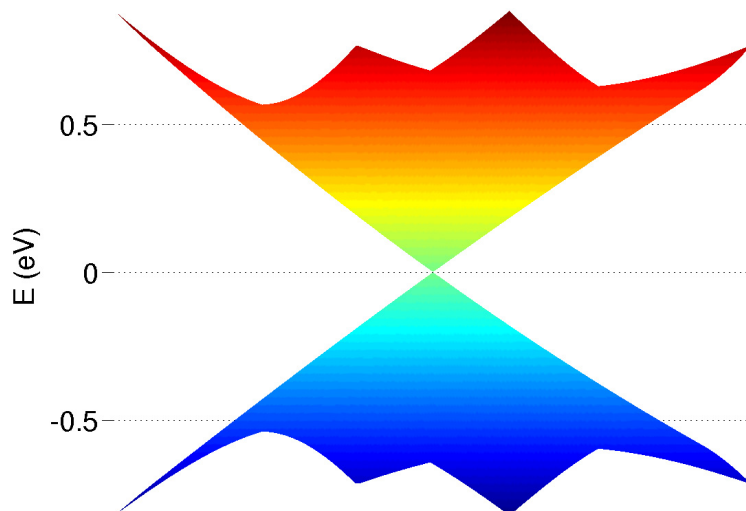


Figure 3.2. A zoom-in on the band structure of graphene around one of the Dirac points.

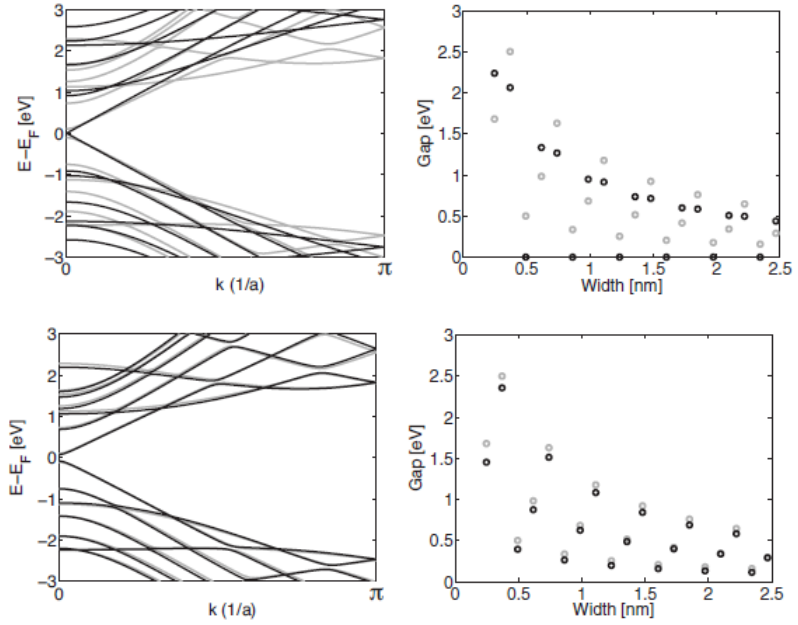


Figure 3.3. Comparison between DFT (gray) and TB (black) results for armchair graphene nanoribbons. The left panel shows the band structure of a 14-AGNR, and right panel a comparison of the calculated the band gaps of narrow AGNRs of different widths. The upper panel compares a nearest-neighbor orthogonal TB model results with the DFT results, and the lower panel a third-nearest neighbor non-orthogonal TB model results with the DFT results.

NRs with different widths. The gray bands and circles have been obtained using DFT simulations, whereas the black ones are from TB calculations. The upper row compares a nearest-neighbor orthogonal TB model with a DFT result, whereas the lower row compares an optimized third-nearest neighbor non-orthogonal TB model with the same DFT result. In the DFT results, the local density approximation has been applied. The parameters are given in Publication I. It can be seen that the nearest-neighbor TB model predicts one third of the ribbons to be metallic, whereas a model with hoppings up to third-nearest neighbors correctly predicts a gap for all AGNRs.

In addition to a different quantization direction, ZGNRs differ from AGNRs by exhibiting a special localized edge state that arises due to the edge topology. Computational results for ZGNRs are shown in Fig. 3.4, where the black lines indicate results from a third-nearest neighbor non-orthogonal mean-field Hubbard model. Interestingly, the localized edge state is located at the CNP and causes all such ribbons to be metallic, in the absence of electron-electron interactions. However, as the DFT or the application of the mean-field Hubbard model show, a gap may open up.

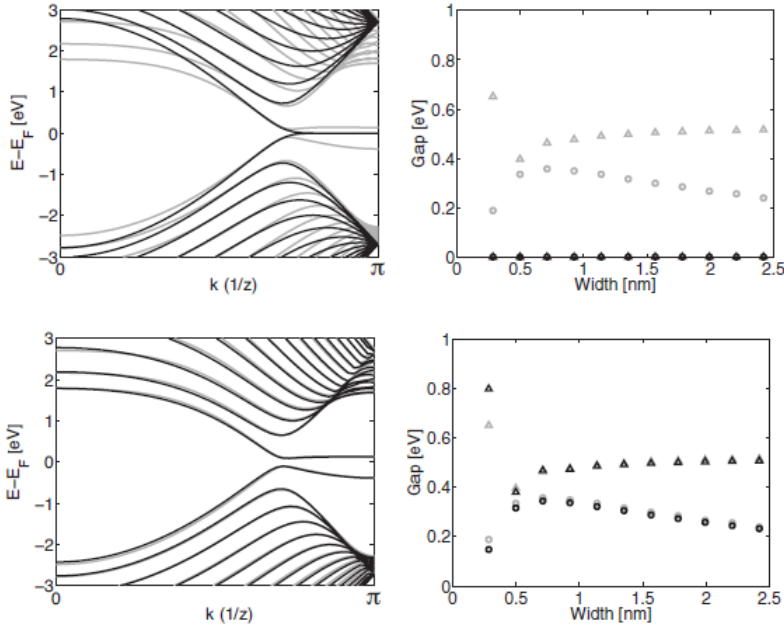


Figure 3.4. Comparison between DFT (gray) and TB (black) results for zigzag graphene nanoribbons. The left panel shows the band structure of a 14-ZGNR, and right panel a comparison of the calculated the band gaps of narrow ZGNRs of different widths. The upper panel compares a nearest-neighbor orthogonal TB model results with the DFT results, and the lower panel a third-nearest neighbor non-orthogonal Hubbard model results with the DFT results.

The opening of the gap depends strongly on the doping of the ribbon, as the simulations predict that only charge-neutral ribbons will have a gap. Thus best comparison with DFT results can be achieved by including a Hubbard mean-field and a parameter set covering electron hoppings and overlaps up to third-nearest neighbors. However, as an overlap matrix complicates the calculations and increases the number of free parameters, without adding significant qualitative detail near the Fermi level, it is not essential in a minimal model. On the other hand, second- and third-nearest neighbor hoppings may be valuable additions in the model. Second-nearest neighbor hopping results in electron-hole asymmetry as well as increased trigonal warping of the conical band structure, whereas third-nearest neighbor hopping causes a band gap in all AGNRs [33]. A TB model with hoppings up to third-nearest neighbors thus is able to accurately reproduce both the *ab initio* band structures and transmission properties of GNRs. The addition Hubbard mean field is relevant mainly for systems containing zigzag-shaped edges, as neither bulk graphene nor armchair-shaped edges exhibit spin-polarization with reasonable values of U .

Ab initio results predict that in AGNRs the edge bond lengths are about 3.5 % shorter than those in the middle of the ribbon, leading to increased overlap and hopping between the corresponding atomic sites. To take this into account in the TB model, it has been proposed that t_1 can be increased by 6–12 % at the edges [32, 34]. The band gaps of AGNRs can be calculated with even better accuracy by taking into account edge relaxation. In ZGNRs the edge relaxation is weaker and modifying the nearest neighbor hopping values to take it into account causes only negligible changes in the band structure.

3.2 Comparisons between simulations and scanning tunneling microscopy results

In scanning tunneling microscopy (STM), an atomically sharp tip is placed on top of a sample, and the electric current is measured after the application of a bias voltage between the sample and the tip. Such a system conducts through quantum-mechanical tunneling of charge carriers. The measured results are affected by the finite lifetime of the charge carriers in the sample, which causes a broadening in energy. In such a case, the tunneling current is proportional to the LDOS of the sample close to the tip. According to the Tersoff-Hamann theory of STM [35],

$$I \propto \sum_{\nu} |\psi_{\nu}(\mathbf{r}_0)|^2 \sigma(E_{\nu} - E_F), \quad (3.1)$$

where $\psi_{\nu}(\mathbf{r}_0)$ is the amplitude of the ν th eigenstate at \mathbf{r}_0 and E_{ν} is the corresponding energy eigenvalue. Thus STM provides a method to study the electronic structure of a sample, as the measured dI/dV maps provide an estimate for the local density of states at the tip position.

In Publication IV, the electronic structure of hexagonal graphene nanoflakes on top of an Ir(111)-surface were studied through STM measurements and computational simulations. The measurements yielded standing wave patterns, whose complexity increased with increasing energy, as shown as in Fig. 3.5 (a). This indicates behavior analogous to a particle-in-a-box-problem. To simulate the patterns, an atomistically exact TB-based model was created, and the eigenstates were solved through exact diagonalization of the TB Hamiltonian. The results are presented in Fig. 3.5 (c), whereas predictions from a simple continuum model based on the Klein-Gordon equation are shown in Fig. 3.5 (d).

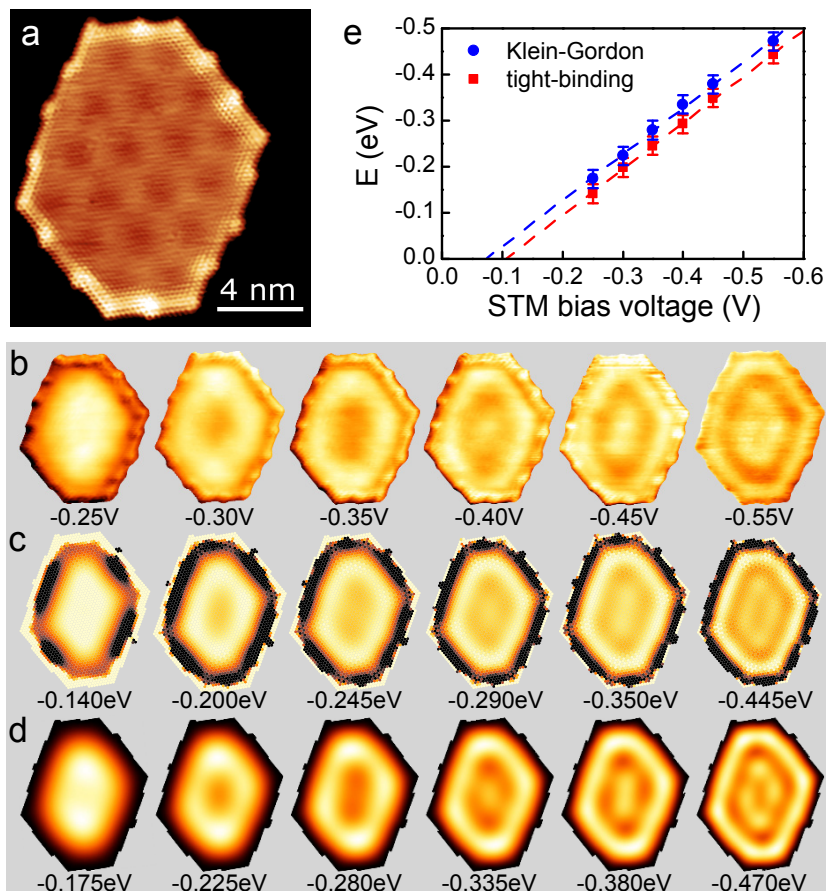


Figure 3.5. (a) Atomically resolved image of a graphene flake on Ir(111). (b) STM maps of graphene nanoflakes on Ir(111), taken at different bias voltages. (c) and (d) show the corresponding TB and continuum model (based on the Klein-Gordon equation) maps. (e) Correspondence between experimental bias voltages and the energy values of the best fitting theoretical simulations.

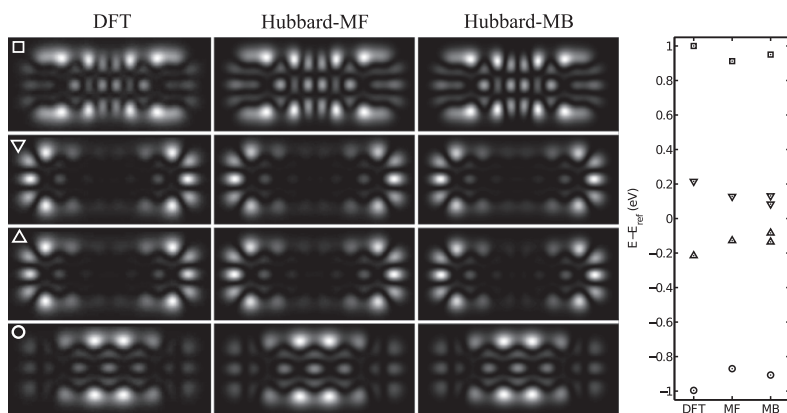


Figure 3.6. Comparison of the low-energy eigenstates (left) and eigenvalues (right) of a finite 7-atom wide AGNR obtained using three different methods. The different markers link the eigenstates and the corresponding eigenvalues.

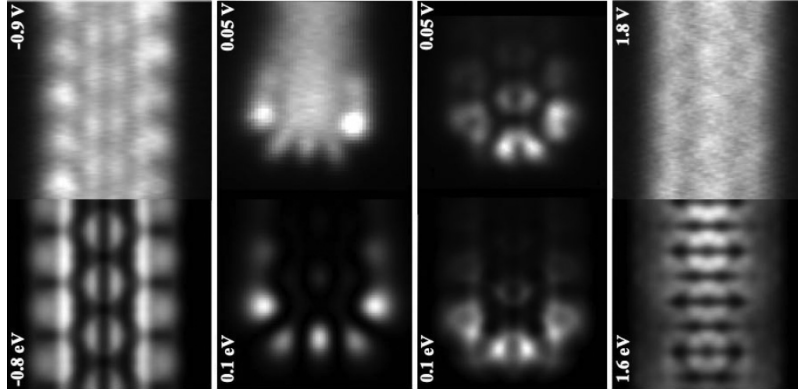


Figure 3.7. Comparison between measured (top) and simulated (bottom) electronic states of finite armchair-edged graphene nanoribbons. These simulations have been performed using the density functional theory, although tight-binding simulations yielded very similar results. In the simulations, the tip is assumed to be a mix between a p -type and an s -type orbital.

Similar confined states have been found also in other studies [36, 37, 38]. In particular, Altenburg et al. [38] argued that the observed states may be examples of confinement of the Ir(111) surface state. This view is supported by *ab initio* calculations, suggesting that the Ir edge state decays slower in the perpendicular direction than bulk graphene states. This can be explained by the fact that the Fermi surface of graphene is located in the vicinity of the K points of the Brillouin zone, whereas the edge state of Ir resides close to the Γ point. On the other hand, one has to note that finite graphene flakes on the Ir(111) substrate were not simulated in Ref. [38] and may exhibit different behavior, especially if their size is small.

Computational results were compared against STM measurements also in Publication II. Finite, seven dimer wide armchair nanoribbons were formed from precursor molecules using a bottom-up technique presented in Ref. [39]. STM imaging and scanning tunneling spectroscopy (STS) measurements of the ribbons was performed, and compared against DFT and Hubbard model results. It was noted that both *ab initio* and Hubbard model calculations can reproduce the low-energy dI/dV maps, measured using both s - and p -type tips. This is illustrated in Fig. 3.6, which compares the theoretical results with each other, and in Fig. 3.7, which compares DFT results with experimental measurements. The simulations are discussed in more detail in Publication III. However, simulating the STS spectra requires a model which takes into account phonon-assisted tunneling, more of which is discussed in Section 4.6.

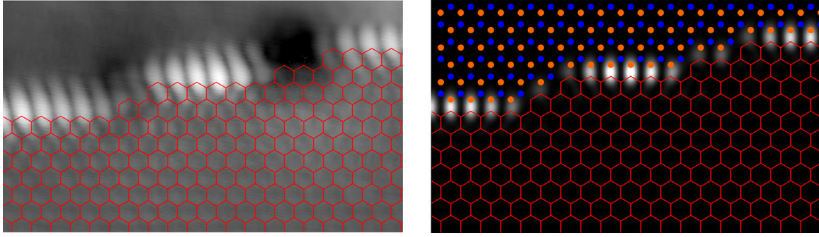


Figure 3.8. Comparison between a measured (left) and a simulated (right) STM map of the graphene - hexagonal boron nitride interface state. The simulated image has been calculated using a third-nearest neighbor TB model. The graphene lattice is indicated by the hexagonal network, whereas the positions of the boron atoms are indicated by orange circles and the positions of the nitrogen atoms by blue circles.

In Publication V the interface between graphene and hexagonal boron nitride (h-BN) was studied. STM measurements showed a series of oblong spots along the interface at low-bias measurements, a feature which according to the simulations matches an interface where the boron and carbon atoms are bonded together. A comparison of the experimental map with a TB simulation is shown in Fig. 3.8. The orthogonal TB model includes hoppings up to third-nearest neighbors, with the hopping parameters being the same for both the graphene and h-BN lattices. h-BN is simulated through onsite potentials on the B and N atoms. The hopping parameters between the graphene and h-BN lattices have been reduced, as this gives a best match with a DFT-based band structure. This is further motivated by DFT predicting longer bond lengths between the two different lattices compared to the intralattice bond lengths. According to both DFT and TB simulations, an interface formed by nitrogen atoms bonding to the graphene edge would look clearly different, as shown in Publication V. Thus it was concluded that the observed interfaces are formed by boron bonding with the carbon atoms along the edge of the graphene lattice.

4. Electronic transport in graphene

The conductance of a device is measured by attaching two or multiple probes, and measuring the current as a function of bias voltage V_b . The conductance is simply obtained from $G = dI/dV_b$. In this Thesis, only two-probe systems are considered. The properties of electronic transport depend heavily on characteristic length scales of the system. The phase coherence length determines the length scale for quantum-mechanical interference phenomena. Scattering by defects with no internal degrees of freedom is elastic, and results in the conservation of the phase of the charge carriers. On the other hand, scattering by other charge carriers or phonons can result in momentum transfer and phase decoherence. The length that sets the scale between scattering events is called the mean free path l , whereas the elastic mean free path l_e sets the scale between elastic scattering events. When l is smaller than the phase coherence length, the corresponding system can be called mesoscopic, and phenomena due to quantum-mechanical interference can be observed. When the size of the system is smaller or at most of the same order as l , the charge carriers behave ballistically or quasi-ballistically.

4.1 Ballistic transport and Fabry-Pérot resonances

One of the most prominent features of graphene is the low amount of disorder present in the material. This is especially true for exfoliated graphene, which may exhibit charge carrier mobilities exceeding 100 000 Vs/cm^2 [9] and ballistic transport in samples that are up to several micrometers long [40]. In 2D graphene, the conductivity σ of a ballistic device is infinite, whereas in a two-terminal device, transverse quantization results in a finite number of transport modes that limit the conductance to $G = G_0 M$, where M is the number of modes. The Landauer-Büttiker for-

malism based on Green's functions yields correctly the quantized conductance of a ballistic graphene device, whereas the Kubo-Greenwood method experiences numerical inaccuracies, as discussed in Publication VI and Ref. [28].

One of the peculiar features of graphene is that ballistic devices with $W \gg L$ exhibit a finite minimum conductivity, even at the Dirac point where the density of states is zero. Theoretically, a minimum conductivity of $4e^2/\pi h$ can be derived, resulting from evanescent modes extending into bulk graphene from the contacts [8, 41]. However, experimental results have yielded larger values than this, which has been attributed to the presence of long-ranged potential disorder due to the substrate [42].

In a ballistic device, scattering of charge carriers is mainly induced by the edges of the sample and the device-contact interfaces. If the system is sufficiently phase coherent, this leads to Fabry-Pérot-type interference of the charge carriers. This was studied in Publication VII, where experimental and simulated results for a suspended graphene device contacted to two metallic leads were compared. According to a particle-in-a-box model for charge carriers with linear dispersion, the conductance of a device with dimensions $W \times L$ should show resonances approximately located at [43, 44]

$$E_{q_L, q_W} \cong \pm \sqrt{E_L^2 (q_L + \delta_L)^2 + E_W^2 (q_W + \delta_W)^2}, \quad (4.1)$$

where $E_L \equiv \hbar v_F/2L$ and $E_W \equiv \hbar v_F/2W$. The values of the constants δ_L and δ_W depend on the details of the interfaces or edges [43], and the quantum numbers q_L and q_W label longitudinal and transverse modes, respectively. Therefore the resonances should roughly occur at intervals of E_L and E_W , with the longitudinal resonances occurring due to bunching of single-mode transverse resonances, thus being of a multimode nature.

Using a nearest-neighbor TB transport model, a device connected to two semi-infinite graphene leads at a constant doping of 1.5 eV was simulated. Figure 4.1 (a) shows the resulting conductance curve, (b) the corresponding $dG/d\mu_0$ map and (c) its Fourier transform. Here μ_0 is a zero-bias chemical potential, roughly corresponding to the gate voltage of an experimental setup. The vertical lines in (a) indicate the positions of the resonances given by Eq. 4.1, whereas the solid and dashed lines in (c) indicate the locations of $1/2E_L$ and $W/L(1/2E_L)$, respectively.

The experimentally measured dI/dV curve showed a similar behavior

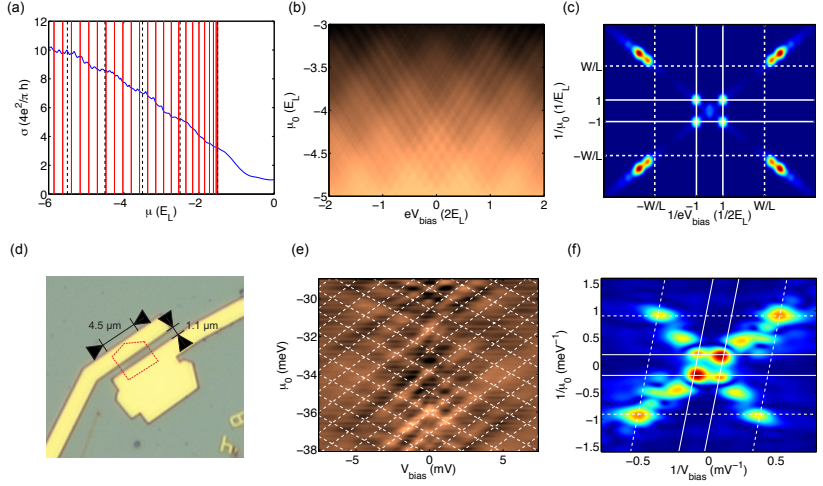


Figure 4.1. (a) Simulated conductance curve, with the vertical lines indicating the positions of single-mode (solid) and multimode (dashed) Fabry-Pérot resonances. (b) Simulated $dG/d\mu_0$ map. (c) Fourier transform of (b). (d) Experimental device consisting of a graphene sample suspended between two metallic contacts. (e) Measured $dG/d\mu_0$ map of the device. (f) Fourier transform of (e).

as the simulations. The resonances were studied quantitatively by converting the gate voltage into a zero-bias chemical potential, after which the plot was differentiated with respect to μ_0 and a Fourier transform was performed. Figures 4.1(d)-(f) show the main results of the analysis. Fig. 4.1(d) shows the experimental setup, (e) the experimental $dG/d\mu_0$ map and (f) the Fourier transform of (b). As in (c), the solid and dashed lines in (f) indicate the locations of $1/2E_L$ and $W/L(1/2E_L)$, respectively.

The Fourier analysis was used to estimate the Fermi velocity in the sample, with a result of $v_F \approx 2.4 \times 10^6$ m/s. The result is significantly higher than what has been measured on a SiO_2 substrate, i.e. roughly 1.4×10^6 m/s [45], or given by a standard DFT model, which is even lower. The discrepancy is explained by electron-electron interactions, which are partly screened on a substrate and not fully taken into account in a plain DFT model. A previous measurement of the Fermi velocity of freestanding graphene yielded a similar result, albeit using a rather different technique based on the cyclotron mass [46].

4.2 Transport in disordered graphene

Transport in disordered graphene is characterized by multiple scattering events, which leads to a drift speed of the charge carriers that is much

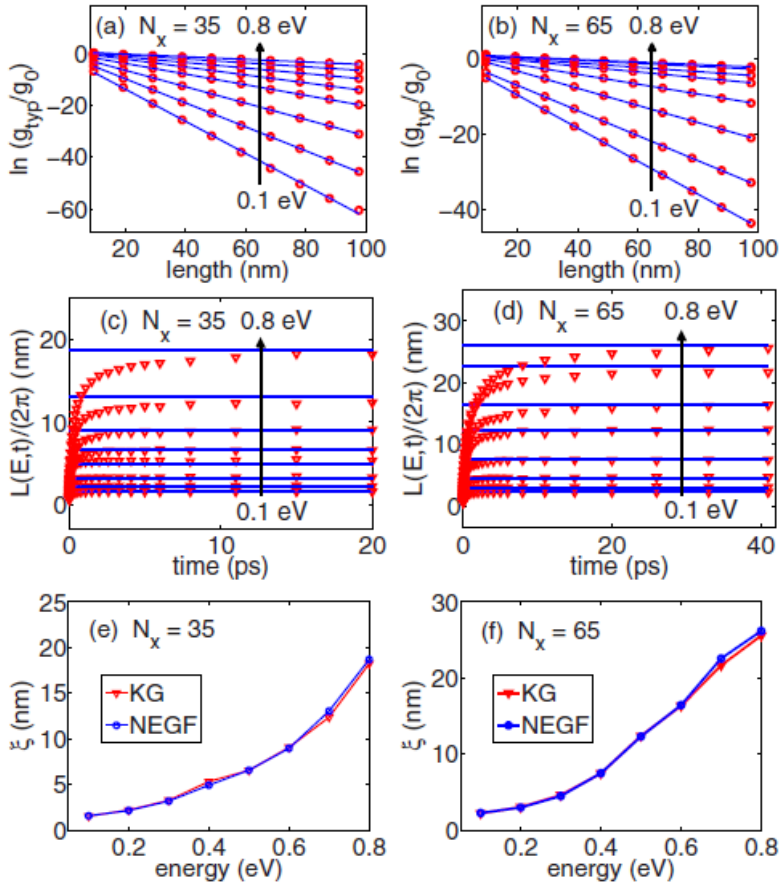


Figure 4.2. Comparison between Kubo-Greenwood and Landauer-Büttiker results. (a) and (b) show exponential fits to the conductances calculated using the Landauer-Büttiker formalism for a 35-atom and a 65-atom wide AGNR, respectively. (c) and (d) show how the Kubo-Greenwood-based propagating lengths (twice the MSD), divided by 2π , converge toward the localization lengths obtained from the results shown in (a) and (b). (e) and (f) show comparisons between estimates for the localization given by the Kubo-Greenwood and Landauer-Büttiker (here called NEGF) methods.

lower than the Fermi velocity. The length scale for this transport regime is set by the electronic mean free path l , i.e. when the system is much larger than l , the charge carriers propagate diffusively.

In the diffusive regime, a conductor follows the classical Ohm's law, i.e. the conductance is directly proportional to the width and inversely proportional to the length of the conductor. However, as mentioned in the previous section, the finite number of conduction channels adds a length-independent resistance to the system, called the contact resistance and equalling $R_c = 1/MG_0$. Thus, in the diffusive regime, the total resistance of the system is $R = R_c + (L/W)\rho$, where ρ is the resistivity, equalling the

inverse of the conductivity σ . Alternatively, this may be written as [20]

$$R(L) = R_c + R_c \frac{L}{l_e}. \quad (4.2)$$

In a diffusive system, the properties of the scatterers thus determine the resistivity of the material.

In a mesoscopic system, corrections to the conductivity arise due to quantum-mechanical interference phenomena. Depending on the material and the type of scattering, interference can lead to either enhanced or decreased backscattering due to constructive or destructive interference between time-reversed propagation paths of the charge carriers. Enhanced backscattering is called localization and decreased backscattering antilocalization. In the presence of disorder that is able to cause scattering between the two independent valleys of the band structure, the charge carriers experience localization, whereas when the disorder causes solely intravalley scattering, the charge carriers experience antilocalization instead. This is typical for graphene in the presence of long-ranged disorder, and has been studied more extensively in e.g. Ref. [47]. Antilocalization causes an increase of the conductivity, whereas localization causes a decrease. The sign of the localization correction to the conductance may be probed using a weak magnetic field, as it will remove the time-reversal symmetry and thus suppress quantum-mechanical interference.

When a phase-coherent system exhibiting localization is sufficiently long, the charge carriers will become strongly localized. In the strongly localized regime, the resistance grows exponentially instead of linearly with the length of the system, i.e. $R \propto \exp(L/\xi)$, with ξ being called the localization length. As a wave packet becomes localized, the mean square displacement given by the KG method will converge to a finite value. In Publication VIII it was shown that the converged MSD given by the Kubo-Greenwood method is directly proportional to the localization length, with the constant of proportionality being approximately $1/\pi$. This is illustrated in Fig. 4.2, which compares KG results with those obtained using Landauer-Büttiker calculations.

4.3 Effective scattering cross-section formalism

The scaling of the conductance of a mesoscopic conductor has been studied extensively for decades, see e.g. Ref. [20]. A useful quantity, called

scattering or transport cross section, can be defined to characterize the scatterers [48]. In Publication IX and Publication X an effective scattering cross section formalism was studied in order to test if single-defect calculations may be used to predict the conductance of a mesoscopic system with a large number of defects. This would enable one to directly apply *ab initio* methods to compute the conductance of realistically sized systems. The scattering cross section s is related to l_e and the concentration of impurities n_{imp} through the relation

$$s(E) = \frac{1}{n_{\text{imp}} l_e(E)}. \quad (4.3)$$

In case of scattering by multiple defect types, the scattering cross sections may be combined based on Matthiessen's rule, which relates the elastic mean free path to the individual elastic mean free paths that correspond to different types of scattering through the reciprocal relation

$$\frac{1}{l_e} = \sum_i \frac{1}{l_{e,i}} \quad (4.4)$$

In principle, Matthiessen's rule could be utilized to also combine the effect of inelastic scattering, but this does not necessarily lead to correct results, as phonons may couple to the defects and impurities present in the lattice.

The mean free path may be used to obtain the conductance of a mesoscopic quasi-1D system through scaling analysis. In the diffusive regime, a relation between l_e and the transmission function can be derived [48] using Eq. 4.2, i.e.

$$l_e(E) = d \frac{N \langle T(E) \rangle}{T_0(E) - \langle T(E) \rangle}, \quad (4.5)$$

where N is the number of scatterers and d the average distance between them. $\langle T(E) \rangle$ is the ensemble averaged transmission function in the presence of scatterers and $T_0(E)$ the ballistic transmission function (equalling the number of conduction channels). Equation 4.5 may be used to derive the expression

$$s(E) = W \frac{T_0(E) - \langle T(E) \rangle}{N \langle T(E) \rangle}, \quad L \ll \xi(E), \quad (4.6)$$

valid in the diffusive transport regime. In principle, with periodic boundary conditions and transverse k -point sampling, one can compute $s(E)$ from single-defect calculations of systems that are small enough to be simulated using the DFT. However, one has to be careful regarding the

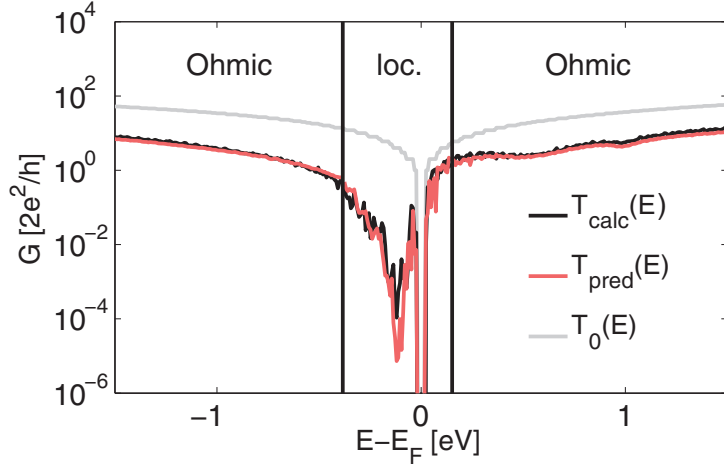


Figure 4.3. Comparison of the calculated and predicted transmission functions for a 30 nm wide and 1000 nm long graphene nanoribbon with a 1% concentration of Stone-Wales defects, 555777 defects and vacancies each. The predicted result is based on a scaling approach utilizing single-defect scattering cross sections. The vertical bars divide the energy range into Ohmic (diffusive) and localized regimes.

condition $L \ll \xi(E)$, as L is not clearly defined in the case of a single-defect calculation. In practice, one needs to construct an expression for $s(E)$ also when the system is in the localized regime. To achieve this, one can approximate that the transmission function is given by $T_{\text{typ}}(E) \simeq T(E_0) \exp(-L/\xi(E))$. This is valid when the contact resistance is negligible compared to the total resistance. Here $T_{\text{typ}} \equiv \exp(\ln T(E))$ is the typical transmission, which is computationally much easier to obtain than the average transmission as the transmission values follow a log-normal distribution in the localized regime [49]. The Thouless relation [50, 51], i.e.

$$\xi(E) = \frac{M+1}{2} l_e(E) \quad (4.7)$$

relates $\xi(E)$ length to l_e . Thus one can derive an expression for $s(E)$ valid in the localized regime:

$$s(E) = \frac{W(T_0(E) + 1) \langle \ln[T_0(E)/T(E)] \rangle}{2N}, \quad L \gg \xi(E). \quad (4.8)$$

In Publication IX, scattering cross sections were calculated using a third-nearest neighbor orthogonal TB model for a Stone-Wales defect, a 555777 defect and a vacancy. A Stone-Wales defect and a 555777 defect are structural defects [52], with the Stone-Wales defect being essentially a bond rotation by 90° resulting in two pentagons and two heptagons embedded in the honeycomb lattice. A 555777 defect is a relaxed form of a divacancy,

consisting of three pentagons and three heptagons. Using the scaling approach based on scattering cross sections, the conductance of a 30 nm wide GNR with a 1% concentration of Stone-Wales defects, 555777 defects and vacancies each was predicted. Applying Matthiessen's rule, the predicted average and typical conductances can be obtained from

$$\langle T(E) \rangle = \frac{T_0(E)}{1 + L \sum_i n_i s_i(E)}, \quad L \ll \xi(E) \quad (4.9)$$

and

$$T_{\text{typ}}(E) = \frac{T_0(E)}{\exp\left[\frac{2L}{T_0(E)+1} \sum_i n_i s_i(E)\right]}, \quad L \gg \xi(E), \quad (4.10)$$

respectively. A comparison of single-defect predictions with simulation results for an ensemble of large systems is shown in Fig. 4.3.

The scattering cross section formalism may be connected to the semi-classical Boltzmann theory of electronic transport. The scattering cross section of a vacancy, or equivalently an infinite onsite potential, can be directly derived from the Boltzmann theory, which predicts a conductance equalling [53]

$$\sigma \approx \frac{2e^2}{h} \frac{2n}{\pi n_{\text{imp}}} \ln^2 \left| \frac{E}{D} \right|, \quad (4.11)$$

where $D = \sqrt{\pi \hbar^2 v_F^2 c}$, with c being the number of carbon atoms per unit area. From Eq. 4.11 one can obtain

$$s(E) = \frac{2D^2}{\Omega \hbar v_F |E|} \ln^{-2} (|E/D|), \quad (4.12)$$

where Ω is the area of the unit cell of the graphene lattice, i.e. $\Omega = 3a_0^2 \cos(\pi/6)/2$. In Fig. 4.4 the analytical scattering cross section has been compared against nearest-neighbor TB results for a system with k -point sampled periodic transverse boundary conditions. One may obtain the correct scattering cross section using Eqs. 4.6 and 4.8 only when the system is purely diffusive or purely localized, respectively. In this case, results for both a diffusive and a localized system had to be used to obtain good values for $s(E)$ without the need of using excessive computational power.

In Publication X, the DFT was applied to obtain *ab initio* scattering cross section for hydrogen, hydroxyl, oxygen, and carbon impurity atoms on graphene. Parametrized TB models for each defect type, optimized against the DFT scattering cross section, were also constructed. Fig. 4.5 shows the results for oxygen (epoxy) and carbon impurities.

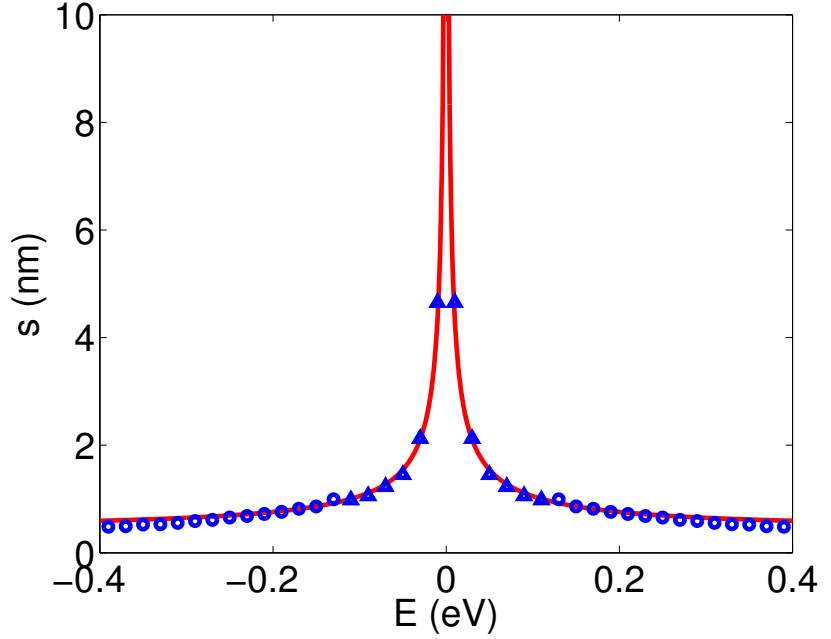


Figure 4.4. Comparison between the scattering cross section given by the Boltzmann formalism, i.e. Eq. 4.12, indicated by the red line, and ensemble-averaged simulated results for a system with k -point sampled periodic transverse boundary conditions. The circles have been obtained simulating a diffusive system and using Eq. 4.6, whereas the triangles have been obtained simulating a localized system and using Eq. 4.8

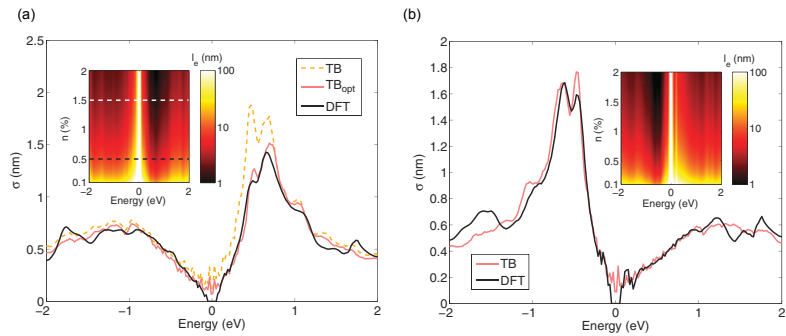


Figure 4.5. Transport scattering cross sections for epoxy (a) and carbon impurities (b). The tight-binding parameters have been optimized to reproduce the DFT result. The insets show the localization lengths as a function of impurity concentration.

4.4 Electronic transport in a magnetic field

Transport in graphene in a magnetic field has been studied in several recent works [54, 55, 56]. If a sufficiently strong external perpendicular magnetic field is applied on a conductor, the system may enter the quantum Hall regime. In the quantum Hall regime, the bulk electronic states in the system become quantized into so-called Landau levels (LLs) [20]. The quantum Hall effect is characterized by the off-diagonal conductance of a multiprobe setup acquiring quantized values, whereas the longitudinal resistance takes non-zero values only at the Landau levels. This is due to the formation of edge channels that propagate in different directions at the opposite edges of the system. Backscattering is possible only at the Landau levels, where the presence of bulk states allows charge carriers to scatter from one edge to another.

In Publication XI the conductance of a two-terminal device was studied in the quantum Hall regime. At high magnetic fields, the spin degeneracy of the charge carriers becomes lifted. However, at lower field strengths the degeneracy of the spins remains, which allowed the use of a non-spin-polarized model. It was found that the type of disorder strongly affects the width of the zeroth Landau level, located at the CNP. With short-ranged potential disorder or vacancy-type defects, the zeroth LL remains delta-function-like, whereas the other LLs become broadened. With longer range potential disorder, the zeroth LL becomes wider, similar to the other LLs. Even if the chemical potential of the system is at a LL, the current flowing through the device, given at zero temperature by [20]

$$I(V_b) = \frac{2e}{h} \int_{E_F - eV_b/2}^{E_F + eV_b/2} T(E) dE, \quad (4.13)$$

is large when the bias window is broad compared to the width of the LL. Thus in an experimental setup, a delta-function like zeroth LL will result in a low measured resistance peak. This agrees with experimental conductance measurements of graphene on a SrTiO₃ substrate [57]. The resistance peak at the zeroth LL was found to decrease significantly as a function of decreasing temperature. In SrTiO₃, the dielectric constant increases by an order of magnitude when the temperature decreases from room to liquid helium temperature. Thus charge inhomogeneities become strongly screened, which according to the simulations will reduce the measured resistance. On the other hand, such a decrease can also be attributed to a reduction in the effects of electron-electron interactions,

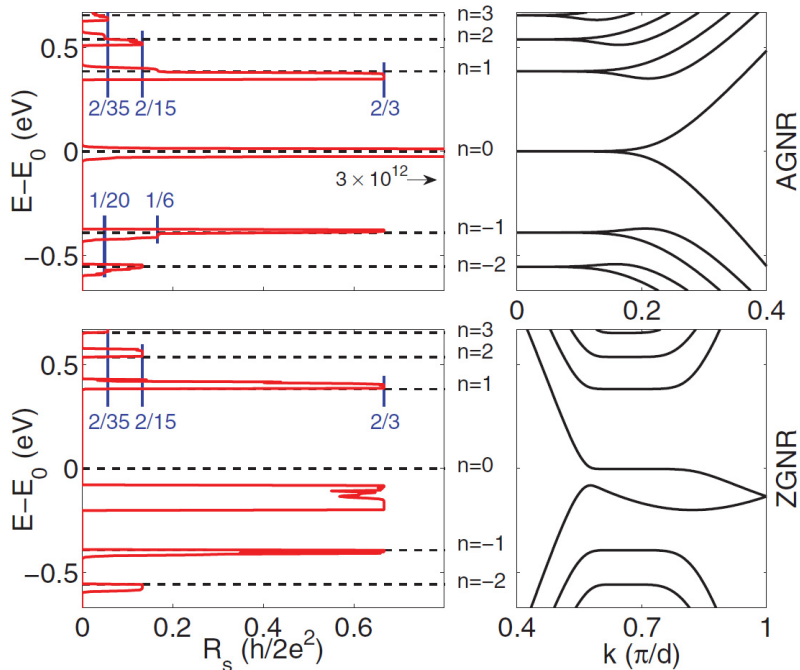


Figure 4.6. Left hand panel: Resistance of AGNRs (top) and ZGNRs in the quantum Hall regime with respect to the location of the zeroth LL E_0 , based on TB simulations. Right hand panel: Corresponding band structures of pristine ribbons.

that will also become more screened with increasing dielectric constant.

In Publication XI, it was also found that at the other LLs, the innermost conduction channels become quickly completely localized in the presence of disorder, whereas the other channels exhibit significantly longer localization lengths. This will lead the four-terminal longitudinal resistance (equalling the total longitudinal resistance minus the contact resistance) to become pinned to fractional values of the resistance quantum at the nonzero LLs, i.e.

$$R = \frac{h}{2e^2} \frac{2}{4n_L^2 - 1}, \quad |n_L| > 0, \quad (4.14)$$

where n_L is the Landau level index. Compared with the experimental results in Ref. [7], the pinned values given by Eq. 4.14 differ by roughly 30% on average.

4.5 Spin-dependent transport

According to theoretical simulations, in a freestanding ZGNR at or very close to half-filling, the edge states are spin-polarized. In the ground

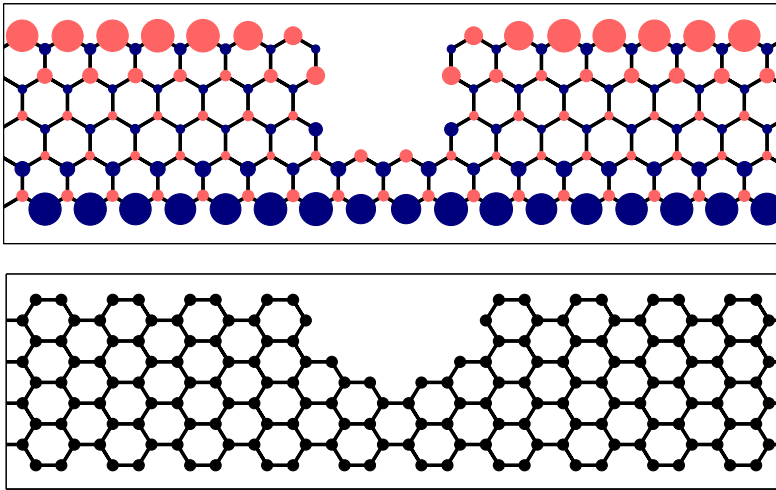


Figure 4.7. The spin polarization of a notched zigzag-edged graphene nanoribbon at half filling. The lower panel shows the atomic structure of the ribbon.

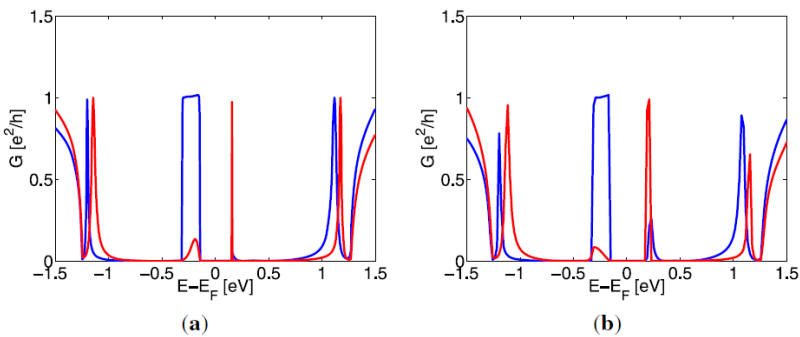


Figure 4.8. Spin-dependent conductance for the notched system shown in Fig. 4.7 computed using (a) tight-binding and (b) DFT. Blue corresponds to the majority spin and red to the minority spin.

state, the opposite edges have opposite majority spin, resulting in symmetric transmission functions for both spin species. However, asymmetry regarding the edges may result in a significantly spin-dependent conductance. In Publication XII, the conductance of a spin-polarized ZGNR with a notch was computed. The structure of the device is shown in Fig. 4.7, which also indicates the spin-polarization of the ground state, computed using the mean-field Hubbard model. It turns out that the transmission function is strongly spin-dependent, as shown in Fig. 4.8. Such a device could be used as a spin-filter. Similar ideas were also presented in Ref. [58]. To realize a spin-filter, it is important that the chemical potential of the system is close to the charge neutrality point and that the applied bias voltage is small, as mean-field Hubbard and DFT calculations indicate that the ground state of a system with even a relatively low level of doping is not spin-polarized. Additionally, the system must be freestanding or located on a substrate that does not affect the edge state or the spin-polarization.

4.6 Phonon-assisted transport

In this section, phonon-assisted tunneling during an STS measurement is studied. In Publication II, experimental STS curves for finite AGNRs on an Au(111) substrate were presented and compared against numerical simulations. Since such ribbons have zigzag-shaped termini, an edge state was observed, as discussed in Section 2.3.2. However, despite good match between simulated and measured STM maps, a simple LDOS-based model did not reproduce the measured STS curves, which revealed in addition to a prominent resonance close to the charge neutrality point, a weaker resonance at positive bias. Interestingly, the weaker resonance disappeared when a bond between the substrate and the opposite end of the molecule was created. In order to explain this, several hypotheses were tested, such as a change of the magnetic polarization or the charging state of the molecule, or a change in the phonon-electron coupling. These hypotheses are discussed in Publication II and Publication III. The best explanation for the observed behavior was found to be that the weaker resonance is a phonon replica of the edge state, with the induced bond suppressing the electron-phonon coupling. This is supported by the fact that the STS spectrum matches well a simulated result with parameterized electron-phonon couplings.

The computations are based on the methods presented in Refs. [59]. If the end state is located at E_0 , the transmission function can be obtained from

$$T(E) \propto \int_{-\infty}^{\infty} \frac{d\sigma}{\hbar} \exp \left(-\frac{\Gamma|\sigma|}{2\hbar} + \frac{2(E - E_0 + \lambda)}{\hbar} - \sum_{\beta} \left| \frac{M_{\beta}}{\hbar\omega_{\beta}} \right|^2 [(1 + 2N_{\omega_{\beta}})(1 - \cos(\omega_{\beta}\sigma)) + i \sin(\omega_{\beta}\sigma)] \right), \quad (4.15)$$

where ω_{β} is the angular frequency of vibrational mode β , $\Gamma = (\Gamma_{\text{tip}} + \Gamma_{\text{substrate}})/2$ is the average coupling strength between the contacts, $\lambda \equiv \sum_{\beta} (M_{\beta}^2/\hbar\omega_{\beta})$ and $N_{\omega_{\beta}}$ is the Bose-Einstein occupation factor. The transmission was computed using a two-phonon model with the electron-phonon coupling strengths M_{β} taken as free parameters and fitted to the measured STS curve, with the results shown in Fig. 4.9(a). However, the values of the parameters M_{β} fit well in the range of *ab initio* results for the electron-phonon coupling strengths in similar but isolated finite nanoribbons, as shown in Fig. 4.9(b).

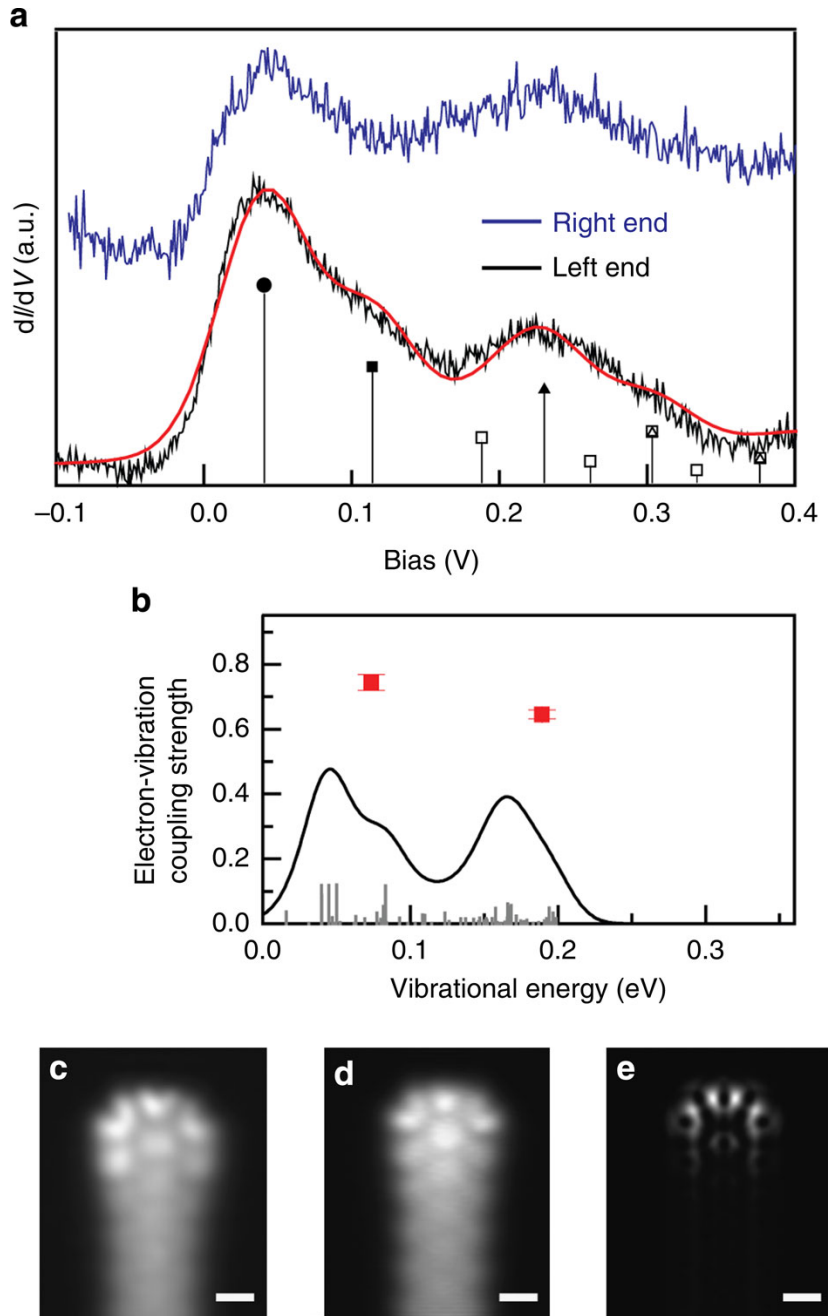


Figure 4.9. (a) Measured STS spectra at the left and right end central atoms of a finite graphene nanoribbon. The red line is a simulated result taking into account interaction with two phonons, with parameters optimized against the measured left end result. (b) Comparison between the optimized parameters for the two phonons and DFT-based results for a similar but shorter molecule. The solid line shows the results with Gaussian broadening. (c) and (d) show constant height STM maps taken at the elastic peak and the replica at 225 meV, respectively, using a CO-terminated tip. (e) DFT simulation of a dI/dV map at the CNP measured with a p -wave tip. A corresponding TB-simulation would yield a very similar result. Scale bars, 0.5 nm.

5. Summary

In this Thesis, the electronic properties of graphene has been studied, with an emphasis on electronic transport. In Publication I, the parameters of the tight-binding model were optimized to reproduce band structure and transport results given by the density functional theory. This model was used in several of the other publications. In Publication II, the local density of states of finite graphene nanoribbons on Au(111) was studied both experimentally and through simulations. The measured and simulated dI/dV maps agreed well with each other, but to obtain a good match with the scanning tunneling spectrum for the end state of the ribbon, phonon-assisted tunneling was needed to be taken into account. Moreover, it was found that the phonon-assisted tunneling is suppressed when the opposite end of the molecule becomes bonded to the substrate. In Publication III, the simulations were presented in more detail, and it was argued that spin-polarization does not seem to be a plausible reason for the observed dI/dV spectrum. Publication III also presented direct comparisons between tight-binding-based and computationally more expensive simulation results, as well as actual measurements, showing that tight-binding gives very accurate results especially for the local density of states of pristine molecules.

In Publication IV, the simulated local density of states for hexagonal graphene nanoflakes was compared against STM measurements performed on an Ir(111) substrate. The results showed a good match between simulations and experimental results, barring the lack of a localized edge state in the experimental results, which can be explained by an interaction between the edges and the substrate. The lower than expected Fermi velocity may be explained by the experimental STM map being affected by direct tunneling between the tip and substrate, as suggested in Ref. [38]. In Publication V the state at the zigzag-shaped between graphene and

hexagonal boron nitride was studied. Comparisons between experimental and simulated scanning tunneling microscopy maps indicated that at the measured interfaces boron atoms were bonded to the graphene edge.

Electronic transport in graphene was studied in several publications. Publication VI presented methods to apply the Kubo-Greenwood method on graphics processing units, significantly increasing the speed of the calculations. Additionally, the Kubo-Greenwood method was explicitly compared with results from the Landauer-Büttiker approach. In Publication VIII, it was shown that the converged value of the propagating length given by the Kubo-Greenwood method is directly proportional to the localization length obtained using the Landauer-Büttiker approach

Transport in ballistic graphene was studied in Publication VII. Experimental measurements indicated the presence of periodic resonances in the dI/dV map, which were attributed to Fabry-Pérot interference. The experimental results matched theoretical simulations in a system with both transverse single-mode resonances and longitudinal multimode resonances, with the estimated Fermi velocity being clearly higher than in graphene on a substrate, thus matching previous results for suspended graphene. In Publication IX a scattering cross section formalism for transport in mesoscopic quasi-1D graphene nanoribbons was studied. It was shown that in addition to diffusive systems, the effective scattering cross-section can accurately be used to estimate the conductance of large-scale localized systems. In principle, the scattering cross section can be obtained from the transmission function of even a single-defect system, provided that the system is either diffusive or localized. This fact was applied in Publication X, where the density functional theory was used to obtain *ab initio* cross sections for various impurities in graphene.

The effect of a strong magnetic field on electronic transport in graphene was studied in Publication XI. It was found that the type of disorder strongly affects the transmission close to the zeroth Landau level. Moreover, it was shown that the innermost conducting channels exhibit very short localization lengths, which may lead the longitudinal resistance peaks to become pinned to fractionally quantized values. Whereas such fractional values have not been found experimentally, a comparison with the measured values found in Ref. [7] shows a difference of only 30 %.

In Publication XII it was found that notched ZGNRs may act as efficient spin filters, although their capability is highly dependent on the size and shape of the notch. Spin filtering devices based on these structures may

be difficult to manufacture, as the edge opposite to the notch needs to be intact and as the spin configuration must remain antiferromagnetic even after a bias voltage is applied.

Bibliography

- [1] K. S. Novoselov, A. K. Geim, S. V. Morozov, D. Jiang, Y. Zhang, S. V. Dubonos, I. V. Grigorieva, and A. A. Firsov, "Electric field effect in atomically thin carbon films," *Science*, vol. 306, p. 666, 2004.
- [2] A. V. Bommel, J. Crombeen, and A. V. Tooren, "LEED and Auger electron observations of the SiC(0001) surface," *Surface Science*, vol. 48, p. 463, 1975.
- [3] A. E. Karu and M. Beer, "Pyrolytic formation of highly crystalline graphite films," *Journal of Applied Physics*, vol. 37, p. 2179, 1966.
- [4] P. R. Wallace, "The Band Theory of Graphite," *Physical Review*, vol. 71, p. 622, 1947.
- [5] A. H. Castro Neto, F. Guinea, N. M. R. Peres, K. S. Novoselov, and A. K. Geim, "The electronic properties of graphene," *Rev. Mod. Phys.*, vol. 81, p. 109, 2009.
- [6] K. S. Novoselov, A. K. Geim, S. V. Morozov, D. Jiang, M. I. Katsnelson, I. V. Grigorieva, S. V. Dubonos, and A. A. Firsov, "Two-dimensional gas of massless Dirac fermions in graphene," *Nature*, vol. 438, p. 197, 2005.
- [7] Y. Zhang, Y.-W. Tan, H. L. Stormer, and P. Kim, "Experimental observation of the quantum Hall effect and Berry's phase in graphene," *Nature*, vol. 438, p. 201, 2005.
- [8] M. I. Katsnelson, "Zitterbewegung, chirality, and minimal conductivity in graphene," *Eur. Phys. J. B*, vol. 51, p. 157, 2006.
- [9] A. Geim and K. Novoselov, "The rise of graphene," *Nat. Mater.*, vol. 6, p. 183, 2007.
- [10] K. Nakada, M. Fujita, G. Dresselhaus, and M. S. Dresselhaus, "Edge state in graphene ribbons: Nanometer size effect and edge shape dependence," *Phys. Rev. B*, vol. 54, p. 17954, 1996.
- [11] M. Y. Han, B. Özyilmaz, Y. Zhang, and P. Kim, "Energy band-gap engineering of graphene nanoribbons," *Phys. Rev. Lett.*, vol. 98, p. 206805, 2007.
- [12] M. Evaldsson, I. V. Zozoulenko, H. Xu, and T. Heinzl, "Edge-disorder-induced anderson localization and conduction gap in graphene nanoribbons," *Phys. Rev. B*, vol. 78, p. 161407, 2008.
- [13] F. Sols, F. Guinea, and A. H. Castro Neto, "Coulomb blockade in graphene nanoribbons," *Phys. Rev. Lett.*, vol. 99, p. 166803, 2007.

- [14] P. Gallagher, K. Todd, and D. Goldhaber-Gordon, "Disorder-induced gap behavior in graphene nanoribbons," *Phys. Rev. B*, vol. 81, p. 115409, 2010.
- [15] S. Reich, J. Maultzsch, C. Thomsen, and P. Ordejón, "Tight-binding description of graphene," *Phys. Rev. B*, vol. 66, p. 035412, 2002.
- [16] P. Hohenberg and W. Kohn, "Inhomogeneous electron gas," *Phys. Rev.*, vol. 136, p. B864, 1964.
- [17] W. Kohn and L. J. Sham, "Self-consistent equations including exchange and correlation effects," *Phys. Rev.*, vol. 140, p. A1133, 1965.
- [18] J. P. Perdew, R. G. Parr, M. Levy, and J. L. Balduz, "Density-functional theory for fractional particle number: Derivative discontinuities of the energy," *Phys. Rev. Lett.*, vol. 49, p. 1691, 1982.
- [19] H. P. Heiskanen, M. Manninen, and J. Akola, "Electronic structure of triangular, hexagonal and round graphene flakes near the Fermi level," *New Journal of Physics*, vol. 10, p. 103015, 2008.
- [20] S. Datta, *Electronic Transport in Mesoscopic Systems*. Cambridge University Press, Cambridge, England, 1997.
- [21] F. Guinea, C. Tejedor, F. Flores, and E. Louis, "Effective two-dimensional Hamiltonian at surfaces," *Phys. Rev. B*, vol. 28, p. 4397, 1983.
- [22] R. Kubo, "Statistical-Mechanical Theory of Irreversible Processes. I. General Theory and Simple Applications to Magnetic and Conduction Problems," *J. Phys. Soc. Jpn.*, vol. 12, p. 570, 1957.
- [23] D. A. Greenwood, "The Boltzmann equation in the theory of electrical conduction in metals," *Proc. Phys. Soc.*, vol. 71, p. 585, 1958.
- [24] D. Mayou, "Calculation of the conductivity in the short-mean-free-path regime," *Europhys. Lett.*, vol. 6, p. 549, 1988.
- [25] D. Mayou and S. N. Khanna, "A real-space approach to electronic transport," *J. Phys. I Paris*, vol. 5, p. 1199, 1995.
- [26] S. Roche and D. Mayou, "Conductivity of quasiperiodic systems: A numerical study," *Phys. Rev. Lett.*, vol. 79, p. 2518, 1997.
- [27] F. Triozon, J. Vidal, R. Mosseri, and D. Mayou, "Quantum dynamics in two- and three-dimensional quasiperiodic tilings," *Phys. Rev. B*, vol. 65, p. 220202, 2002.
- [28] T. Markussen, R. Rurali, M. Brandbyge, and A.-P. Jauho, "Electronic transport through si nanowires: Role of bulk and surface disorder," *Phys. Rev. B*, vol. 74, p. 245313, 2006.
- [29] N. Leconte, A. Lherbier, F. Varchon, P. Ordejon, S. Roche, and J.-C. Charlier, "Quantum transport in chemically modified two-dimensional graphene: From minimal conductivity to Anderson localization," *Phys. Rev. B*, vol. 84, p. 235420, 2011.
- [30] T. M. Radchenko, A. A. Shylau, and I. V. Zozoulenko, "Influence of correlated impurities on conductivity of graphene sheets: Time-dependent real-space Kubo approach," *Phys. Rev. B*, vol. 86, p. 035418, 2012.

- [31] A. Lherbier, S. M.-M. Dubois, X. Declerck, Y.-M. Niquet, S. Roche, and J.-C. Charlier, “Transport properties of graphene containing structural defects,” *Phys. Rev. B*, vol. 86, p. 075402, 2012.
- [32] Y.-W. Son, M. L. Cohen, and S. G. Louie, “Energy gaps in graphene nanoribbons,” *Phys. Rev. Lett.*, vol. 97, p. 216803, 2006.
- [33] D. Gunlycke, D. Areshkin, J. Li, J. W. Mintmire, and C. White, “Hidden one-electron interactions in carbon nanotubes revealed in graphene nanostrips,” *Nano Lett.*, vol. 7, p. 825, 2007.
- [34] D. Gunlycke and C. T. White, “Tight-binding energy dispersions of armchair-edge graphene nanostrips,” *Phys. Rev. B*, vol. 77, p. 115116, 2008.
- [35] J. Tersoff and D. R. Hamann, “Theory of the scanning tunneling microscope,” *Phys. Rev. B*, vol. 31, p. 805, 1985.
- [36] D. Subramaniam, F. Libisch, Y. Li, C. Pauly, V. Geringer, R. Reiter, T. Mashoff, M. Liebmann, J. Burgdörfer, C. Busse, T. Michely, R. Mazzarello, M. Pratzer, and M. Morgenstern, “Wave-function mapping of graphene quantum dots with soft confinement,” *Phys. Rev. Lett.*, vol. 108, p. 046801, 2012.
- [37] S.-H. Phark, J. Borme, A. L. Vanegas, M. Corbetta, D. Sander, and J. Kirschner, “Direct observation of electron confinement in epitaxial graphene nanoislands,” *ACS Nano*, vol. 5, p. 8162, 2011.
- [38] S. J. Altenburg, J. Kröger, T. O. Wehling, B. Sachs, A. I. Lichtenstein, and R. Berndt, “Local gating of an Ir(111) surface resonance by graphene islands,” *Phys. Rev. Lett.*, vol. 108, p. 206805, 2012.
- [39] J. Cai, P. Ruffieux, R. Jaafar, M. Bieri, B. T. S. Blankenburg, M. Muoth, A. P. Seitsonen, M. Saleh, X. Feng, K. Mullen, and R. Fasel, “Atomically precise bottom-up fabrication of graphene nanoribbons,” *Nature*, vol. 466, p. 470, 2010.
- [40] C. Berger, Z. Song, X. Li, X. Wu, N. Brown, C. Naud, D. Mayou, T. Li, J. Hass, A. N. Marchenkov, E. H. Conrad, P. N. First, and W. A. de Heer, “Electronic confinement and coherence in patterned epitaxial graphene,” *Science*, vol. 312, p. 1191, 2006.
- [41] J. Tworzydło, B. Trauzettel, M. Titov, A. Rycerz, and C. Beenakker, “Sub-Poissonian Shot Noise in Graphene,” *Phys. Rev. Lett.*, vol. 96, p. 246802, 2006.
- [42] S. Das Sarma, S. Adam, E. H. Hwang, and E. Rossi, “Electronic transport in two-dimensional graphene,” *Rev. Mod. Phys.*, vol. 83, pp. 407–470, 2011.
- [43] D. Gunlycke and C. T. White, “Graphene interferometer,” *Appl. Phys. Lett.*, vol. 93, p. 2106, 2008.
- [44] M. Müller, M. Bräuninger, and B. Trauzettel, “Temperature Dependence of the Conductivity of Ballistic Graphene,” *Phys. Rev. Lett.*, vol. 103, p. 196801, 2009.
- [45] Y. Zhang, V. W. Brar, C. Girit, A. Zettl, and M. F. Crommie, “Origin of spatial charge inhomogeneity in graphene,” *Nat. Phys.*, vol. 5, p. 722, 2009.

- [46] D. C. Elias, R. V. Gorbachev, A. S. Mayorov, S. V. Morozov, A. A. Zhukov, P. Blake, L. A. Ponomarenko, I. V. Grigorieva, K. S. Novoselov, F. Guinea, and A. K. Geim, “Dirac cones reshaped by interaction effects in suspended graphene,” *Nat. Phys.*, vol. 7, p. 701, 2011.
- [47] J. Wurm, M. Wimmer, and K. Richter, “Symmetries and the conductance of graphene nanoribbons with long-range disorder,” *Phys. Rev. B*, vol. 85, p. 245418, 2012.
- [48] T. Markussen, R. Rurali, X. Cartoixa, A.-P. Jauho, and M. Brandbyge, “Scattering cross section of metal catalyst atoms in silicon nanowires,” *Phys. Rev. B*, vol. 81, p. 125307, 2010.
- [49] P. W. Anderson, D. J. Thouless, E. Abrahams, and D. S. Fisher, “New method for a scaling theory of localization,” *Phys. Rev. B*, vol. 22, p. 3519, 1980.
- [50] D. J. Thouless, “Localization distance and mean free path in one-dimensional disordered systems,” *Journal of Physics C: Solid State Physics*, vol. 6, p. L49, 1973.
- [51] C. W. J. Beenakker, “Random-matrix theory of quantum transport,” *Rev. Mod. Phys.*, vol. 69, pp. 731–808, 1997.
- [52] F. Banhart, J. Kotakoski, and A. V. Krasheninnikov, “Structural defects in graphene,” *ACS Nano*, vol. 5, p. 26, 2011.
- [53] T. O. Wehling, S. Yuan, A. I. Lichtenstein, A. K. Geim, and M. I. Katsnelson, “Resonant scattering by realistic impurities in graphene,” *Phys. Rev. Lett.*, vol. 105, p. 056802, 2010.
- [54] J. Jung and A. H. MacDonald, “Theory of the magnetic-field-induced insulator in neutral graphene sheets,” *Phys. Rev. B*, vol. 80, p. 235417, 2009.
- [55] R. Ribeiro, J.-M. Poumirol, A. Cresti, W. Escoffier, M. Goiran, J.-M. Broto, S. Roche, and B. Raquet, “Unveiling the magnetic structure of graphene nanoribbons,” *Phys. Rev. Lett.*, vol. 107, p. 086601, 2011.
- [56] D. Soriano, N. Leconte, P. Ordejón, J.-C. Charlier, J.-J. Palacios, and S. Roche, “Magnetoresistance and magnetic ordering fingerprints in hydrogenated graphene,” *Phys. Rev. Lett.*, vol. 107, p. 016602, 2011.
- [57] N. J. G. Couto, B. Sacépé, and A. F. Morpurgo, “Transport through graphene on SrTiO₃,” *Phys. Rev. Lett.*, vol. 107, p. 225501, 2011.
- [58] M. Wimmer, I. Adagideli, S. Berber, D. Tománek, and K. Richter, “Spin currents in rough graphene nanoribbons: Universal fluctuations and spin injection,” *Phys. Rev. Lett.*, vol. 100, p. 177207, 2008.
- [59] N. S. Wingreen, K. W. Jacobsen, and J. W. Wilkins, “Inelastic scattering in resonant tunneling,” *Phys. Rev. B*, vol. 40, p. 11834, 1989.



ISBN 978-952-60-5814-6
ISBN 978-952-60-5815-3 (pdf)
ISSN-L 1799-4934
ISSN 1799-4934
ISSN 1799-4942 (pdf)

Aalto University
School of Science
Department of Applied Physics
www.aalto.fi

**BUSINESS +
ECONOMY**

**ART +
DESIGN +
ARCHITECTURE**

**SCIENCE +
TECHNOLOGY**

CROSSOVER

**DOCTORAL
DISSERTATIONS**